

1      **Investigating temporal characteristics of polarimetric and electrical**  
2      **signatures in three severe storms: Insights from the VORTEX-Southeast**  
3      **field campaign**

4      Milind Sharma<sup>a</sup>, Robin L. Tanamachi<sup>a</sup>, and Eric C. Bruning<sup>b</sup>

5      <sup>a</sup>*Department of Earth, Atmospheric, and Planetary Sciences, Purdue University, West Lafayette,*  
6      *Indiana, USA*

7      <sup>b</sup>*Department of Geosciences, Texas Tech University, Lubbock, Texas, USA*

8      *Corresponding author:* Milind Sharma, milindsharma@tamu.edu

9      Current affiliation: Department of Atmospheric Sciences, Texas A&M University, College Station,  
10     Texas, USA

<sup>11</sup> ABSTRACT: The dual-polarization radar characteristics of severe storms are commonly used as  
<sup>12</sup> indicators to estimate the size and intensity of deep convective updrafts. In this study, we track rapid  
<sup>13</sup> fluctuations in updraft intensity and size by objectively identifying polarimetric fingerprints such  
<sup>14</sup> as  $Z_{DR}$  and  $K_{DP}$  columns, which serve as proxies for mixed-phase updraft strength. We quantify  
<sup>15</sup> the volume of  $Z_{DR}$  and  $K_{DP}$  columns to evaluate their utility in diagnosing temporal variability  
<sup>16</sup> in lightning flash characteristics. Specifically, we analyze three severe storms that developed in  
<sup>17</sup> environments with low-to-moderate instability and strong 0–6 km wind shear in northern Alabama  
<sup>18</sup> during the 2016-17 VORTEX-Southeast field campaign. In these three cases (a tornadic supercell  
<sup>19</sup> embedded in stratiform precipitation, a nontornadic supercell, and a supercell embedded within a  
<sup>20</sup> quasi-linear convective system), we find that the volume of the  $K_{DP}$  columns exhibits a stronger  
<sup>21</sup> correlation with the total flash rate . The higher covariability of  $K_{DP}$  column volume with total flash  
<sup>22</sup> rate suggests that the overall electrification and precipitation microphysics was dominated by cold  
<sup>23</sup> cloud processes. The lower covariability with  $Z_{DR}$  column volume indicates the presence of non-  
<sup>24</sup> steady updrafts or a less prominent role of warm rain processes in graupel growth and subsequent  
<sup>25</sup> electrification. Furthermore, we observe that the majority of cloud-to-ground (CG) lightning  
<sup>26</sup> strikes carried negative charge to the ground. In contrast to findings from a tornadic supercell over  
<sup>27</sup> the Great Plains, lightning flash initiations in the Alabama storms primarily occurred outside the  
<sup>28</sup> footprint of the  $Z_{DR}$  and  $K_{DP}$  column objects.

31 SIGNIFICANCE STATEMENT: This study quantifies the correlation between mixed-phase up-  
32 draft intensity and total lightning flash rate in three severe storms in northern Alabama. In the  
33 absence of direct updraft velocity measurements, we use polarimetric signatures, such as  $Z_{DR}$  and  
34  $K_{DP}$  columns, as proxies for updraft strength. Our analysis of polarimetric radar and lightning  
35 mapping array data reveals that lightning flash rate is more highly correlated with  $K_{DP}$  column  
36 volume than with  $Z_{DR}$  column volume in all three storms examined. This contrasts with previous  
37 findings in storms over the central Great Plains, where  $Z_{DR}$  column volume showed higher covari-  
38 ability with flash rate. Interestingly, lightning initiation in the Alabama storms mainly occurred  
39 outside the  $Z_{DR}$  and  $K_{DP}$  column areas, contrary to previous findings.

40 **1. Introduction**

41 Linking the dynamics of moist deep convective updrafts with microphysical processes has been a  
42 challenging task both in terms of observational analyses and numerical simulations. While remote  
43 sensing techniques enable tracking of spatiotemporal evolution of the morphology, intensity, and  
44 precipitation processes within thunderstorms, they often lack validation against *in situ* observa-  
45 tions. On the other hand, high-resolution numerical modeling tools have the ability to explicitly  
46 simulate convection, but microphysical processes are still parameterized. Radar observations help  
47 improve bulk microphysics parameterization schemes by constraining the parameters of particle  
48 size distribution for hydrometeors involved in warm and cold cloud processes. However, the chal-  
49 lenges associated with low-order moment representation in bulk microphysics schemes often result  
50 in large uncertainties in estimates of microphysical processes such as evaporation, sedimentation,  
51 riming, melting, and sublimation (Morrison et al. 2020). These uncertainties carry forward to the  
52 radar observation operators used to simulate polarimetric signatures associated with deep convec-  
53 tive updraft strength, such as differential reflectivity ( $Z_{DR}$ ) and specific differential phase ( $K_{DP}$ )  
54 columns derived from numerical weather model output. As a consequence, detailed weather radar  
55 observations remain crucial to improve our understanding of the coupling between convective  
56 dynamics and storm microphysics.

57 Unlike classic supercells in the high-CAPE environments of the central Great Plains, forecasting  
58 and nowcasting severe weather risk for non-classic tornadic storms (NCTS), is a challenging task

---

29 This Work has been accepted to Monthly Weather Review. The AMS does not guarantee that the copy provided here is an accurate copy of the  
30 Version of Record (VoR).

(Dean 2008; Schneider and Dean 2008; Dean and Schneider 2012). Multi-scale interactions all the way from synoptic (pretornadic frontogenesis) to meso- $\beta$  scale can result in rapid destabilization occurring within a few hours before convection initiation, often on spatiotemporal scales that are unresolvable by conventional observations (Sherburn and Parker 2014; Sherburn et al. 2016; King et al. 2017; Chasteen and Koch 2022a,b). In nonsupercellular severe convective storms, WSR-88Ds are most effective at identifying tornadic risk within a range of less than 60 km and with lead times as short as 10 minutes (Davis and Parker 2014; Goodnight et al. 2022). Alternatively, satellite and ground-based observations of the intensity and width of convective updrafts and lightning flash rates have been useful to discriminate between nonsevere and significantly severe storms at longer lead times (Bedka et al. 2015; Gravelle et al. 2016; Sandmæl et al. 2019; Mecikalski et al. 2021). The intensity of convective updrafts is also known to influence the storm charge structure, flash size, and the associated lightning flash rate through modulation of microphysical processes such as precipitation pathways and cloud glaciation (Marshall et al. 1995; Goodman et al. 2005; Deierling et al. 2008; Deierling and Petersen 2008; Bruning and MacGorman 2013; Bruning et al. 2014; Fridlind et al. 2019). The motivation for this study is driven by the strong connection between storm electrification and mixed-phase microphysical processes. We aim to investigate the covariability between polarimetric signatures of mixed-phase microphysics (specifically  $Z_{DR}$  and  $K_{DP}$  columns), which are reliable indicators of deep convective updrafts, and total lightning flash rates in three severe storms observed during the VORTEX-Southeast (VORTEX-SE or VSE) field campaign.

$Z_{DR}$  columns are microphysical features that form due to vertical size-sorting of drops dominated by warm-rain precipitation processes in the early stages of deep convective updraft life cycle. During the initial phase,  $Z_{DR}$  columns above the environmental 0°C level are composed of low concentration of large (> 2 mm) raindrops. Collision and coalescence of cloud droplets as well as accretion of cloud droplets by raindrops can result in large (> 4–5 mm) raindrops, expanding the  $Z_{DR}$  column downward from above (Kumjian et al. 2014). During the mature phase, smaller raindrops and/or those within stronger updraft regions are lofted upwards into the mixed-phase region and grow by coalescence and accretion, thereby expanding  $Z_{DR}$  columns above. Drops ascending to higher altitudes soon reach their nucleation temperature and begin to freeze, with these partially frozen drops serving as embryos for hailstones growing in wet regime. As supercooled raindrops

begin to freeze at higher altitudes and mix with water-coated graupel and hail, the  $Z_{DR}$  values decrease. This decrease demarcates the top of the  $Z_{DR}$  column, making it easier to distinguish the columnar protrusion of enhanced  $Z_{DR}$  values against the background. The  $Z_{DR}$  column is thus capped by reduced values of co-polar cross correlation coefficient ( $\rho_{hv}$ ) and enhanced linear depolarization ratio (Kumjian et al. 2012, 2014). As updrafts become weaker and wet hailstones occupying a higher fraction of mixed-phase precipitation scavenge supercooled drops, the  $Z_{DR}$  columns begin to collapse.  $K_{DP}$  columns on the other hand, are primarily associated with high concentration of (oriented nonspherical) mixed-phase hydrometeors (e.g., wet hailstones) and drops shed from hailstones growing in a wet regime (Hubbert et al. 1998; Loney et al. 2002; Schlatter 2003), a process tied to cold cloud microphysics, which usually occurs later in the life cycle of a deep convective storm.  $Z_{DR}$  and  $K_{DP}$  columns may be spatially offset at low levels, but the two often overlap at mid-levels (Crowe et al. 2012; Loeffler and Kumjian 2020).

Warm rain dominates radar scattering amplitudes in the  $Z_{DR}$  columns and wet/mixed-phase hydrometeors dominate scattering in the  $K_{DP}$  columns (Loney et al. 2002). As a result, it is possible to determine the microphysical state of an updraft based on the evolution of  $Z_{DR}$  and  $K_{DP}$  columns. An increasing trend in the  $K_{DP}$  column volume either indicates a high liquid water content (LWC) or enhanced wet growth of non-spherical ice. An air parcel ascending along a moist adiabat in an updraft with high LWC likely has a relative humidity close to water supersaturation, promoting riming of ice crystals and graupel, and leading to the growth of wet/mixed-phase hydrometeors (Hueholt et al. 2022). Therefore, rapid accretion of cloud liquid by ice particles at the onset of cloud glaciation, particularly at warmer temperatures, would contribute to a more pronounced  $K_{DP}$  column signature in the radar data. If lightning flash rates increase in tandem with the  $K_{DP}$  column volume, it is likely that the overall electrification and precipitation microphysics is dominated by cold cloud processes. On the other hand, warm rain processes that contribute to the formation of  $Z_{DR}$  columns can dominate graupel growth and storm electrification only if collision-coalescence begins before cloud glaciation occurs (Phillips 2024). This scenario is more likely during periods of rapid intensification of storm updrafts in deep convective clouds with a significant warm cloud depth or a delayed glaciation in the mixed-phase region. This is because stronger vertical velocities are required for size sorting of cloud condensate, leading to the formation of a  $Z_{DR}$  column. Thus,

<sup>118</sup> covarying  $Z_{DR}$  column volume and lightning flash rates may suggest that warm rain processes are  
<sup>119</sup> actively involved in graupel production and storm electrification.

<sup>120</sup> The temporal evolution of  $Z_{DR}$  and  $K_{DP}$  columns is representative of the time-integrated mi-  
<sup>121</sup> crophysical state of mixed-phase hydrometeors encompassing all prior interactions and processes  
<sup>122</sup> affecting the hydrometeor growth, which collectively contribute to the radar scattering amplitude.  
<sup>123</sup> As a result, the changes in the properties of  $Z_{DR}$  and  $K_{DP}$  columns occur over a time scale of at  
<sup>124</sup> least a few minutes in deep convective updrafts. This time scale is inherently slower compared to  
<sup>125</sup> the rapid response of storm kinematics (less than 1 minute) to variations in pressure gradients and  
<sup>126</sup> updraft buoyancy. Additionally, the time scale of flash-initiating electric fields is often influenced  
<sup>127</sup> by turbulent eddies and is likely of the same order as storm kinematics (Salinas et al. 2022). We  
<sup>128</sup> hypothesize that the mismatch in the time scale of evolution of the microphysical state and lightning  
<sup>129</sup> flash rates can still provide useful information about the corresponding slow and fast responses of  
<sup>130</sup> updraft kinematics to cloud dynamical and microphysical processes.

<sup>131</sup> The presence of a deep and persistent rotating updraft, known as a mesocyclone in supercells  
<sup>132</sup> (Doswell and Burgess 1993), enables the efficient transport of large amounts of supercooled liquid  
<sup>133</sup> cloud droplets to the mixed-phase region ( $0^{\circ}$  to  $-40^{\circ}\text{C}$ ). The abundant supply of supercooled water  
<sup>134</sup> is conducive to the formation of  $Z_{DR}$  and  $K_{DP}$  columns as well as charge separation between  
<sup>135</sup> ice crystals and graupel. The rearrangement of oppositely charged ice particles gives rise to  
<sup>136</sup> local pockets of high charge density generating a net electric field that can intensify further in  
<sup>137</sup> the presence of small-scale turbulent eddies at the updraft-downdraft interface or in regions with  
<sup>138</sup> horizontal gradients in vertical velocity (Calhoun et al. 2014; Stough et al. 2021; Souza and  
<sup>139</sup> Bruning 2021; Stough et al. 2022). Substantial gaps in low-level NEXRAD coverage pose a  
<sup>140</sup> challenge for high-quality vertical velocity retrieval through multi-Doppler radar analysis. As  
<sup>141</sup> a result, obtaining reliable estimates of updraft intensity can be a difficult task during real-time  
<sup>142</sup> warning and forecast operations that heavily rely on live radar data for situational awareness  
<sup>143</sup> and warning decision support. To bridge this gap, we leverage polarimetric signatures linked  
<sup>144</sup> to mid-level updraft strength, such as  $Z_{DR}$  and  $K_{DP}$  columns, to investigate whether an increase  
<sup>145</sup> in the volume of these columns correlates with higher total lightning flash rates. An increase  
<sup>146</sup> in the mass flux of both precipitating and nonprecipitating ice species (graupel and ice crystals,  
<sup>147</sup> respectively) would indicate an enhanced charge separation and an increase in lightning flash rate

through the noninductive charging mechanism (Reynolds et al. 1957; Takahashi 1978; Kuettner et al. 1981; Williams 1985; Latham and Dye 1989; Carey and Rutledge 2000). The polarimetric signatures are readily available with each WSR-88D volume scan and do not require extensive manual postprocessing or quality control. Furthermore, both  $Z_{DR}$  and  $K_{DP}$  columns may serve as reliable indicators of the underlying warm and cold-phase microphysical processes, and changes in the areal extent of the column and altitude above the environmental  $0^{\circ}\text{C}$  level have been used to infer qualitative changes in updraft strength, making them effective proxies for assessing the strength of mixed-phase updrafts (Picca 2010; Kumjian et al. 2012; Snyder et al. 2015; Van Den Broeke 2016, 2017, 2020; French and Kingfield 2021; Segall et al. 2022; Wilson and Van Den Broeke 2022). Ryzhkov et al. (1994) suggested that the  $Z_{DR}$  columns can be used to infer the location of updrafts when only single-Doppler radar data are available. Kumjian et al. (2014) found positive correlation between  $Z_{DR}$  column height and updraft strength in their numerical simulations and suggested that the former could be used as an indicator of storm severity. Snyder et al. (2017) found a high correlation between the depth of the  $K_{DP}$  columns and maximum vertical velocity above the  $K_{DP}$  columns and even suggested  $K_{DP}$  to be a better alternative for locating updrafts at higher frequencies (e.g., X-band radars) to avoid complicated biases in  $Z_{DR}$  field caused by high differential attenuation.

Even though the anatomy of  $Z_{DR}$  and  $K_{DP}$  columns is not identical, *in situ* and radar observations of elevated  $Z_{DR}$  and  $K_{DP}$  values above the environmental  $0^{\circ}\text{C}$  level have repeatedly shown that these columnar extensions are either adjacent to or collocated with convective updrafts in ordinary and multicellular thunderstorms (Hall et al. 1984; Taylor and Illingworth 1987; Illingworth et al. 1987; Bringi et al. 1991; Brandes et al. 1995; Bringi et al. 1996, 1997; Smith et al. 1999; Knight 2006; van Lier-Walqui et al. 2016; Plummer et al. 2018) as well as supercells in high instability environments (e.g., Conway and Zrnić 1993; Hubbert et al. 1998; Loney et al. 2002; Kumjian and Ryzhkov 2008; Snyder et al. 2013). Kumjian et al. (2010) highlighted a competing effect between the spatial footprint of  $Z_{DR}$  and  $K_{DP}$  columns at the environmental freezing level within a cyclic nontornadic supercell. They identified repeated cycles where the  $Z_{DR}$  column footprint expanded with intensifying updrafts, coinciding with a reduction in the  $K_{DP}$  column area. Conversely, when the  $K_{DP}$  column expanded, it corresponded to a contraction of the  $Z_{DR}$  column, resulting in a more significant overlap between their spatial footprints. This increased overlap was attributed to

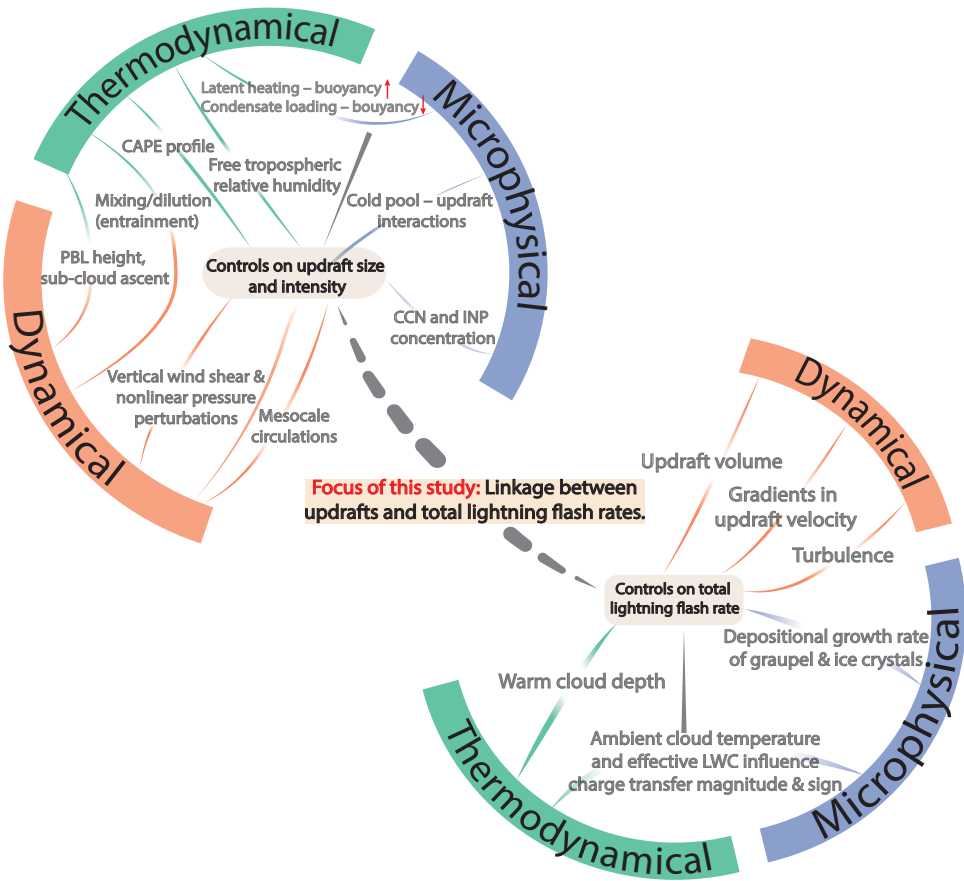
178 precipitation fallout caused by weaker updraft vertical velocity, which was insufficient for vertical  
179 size sorting of hydrometeors, as well as the presence of larger hail, both of which contributed to  
180 the shrinkage of  $Z_{DR}$  column. Strapp et al. (2016) studied ice particle formation in deep convective  
181 clouds and found that a large concentration of partially frozen droplets in the mixed-phase region  
182 favored the rapid growth of ice particles by depleting more water vapor than coexistent droplets. The  
183 authors suggested that the ice particle growth thus becomes sensitive to local thermodynamics and  
184 vertical velocity, eventually affecting the phase composition and size distribution of ice particles.  
185 Johnson (1987) demonstrated that a graupel particle is particularly efficient at accreting cloud  
186 liquid relative to a raindrop of the same mass initially, owing to its lower bulk density and wider  
187 cross-sectional area. By extension, ice crystals and snowflakes would be even more efficient at  
188 accreting cloud liquid. The slower fall speed of ice particles allows for longer suspension in the  
189 updraft against gravity effects. Therefore, a weak or non-steady updraft in an environment with  
190 a relatively shallow warm cloud depth can promote more ice particle growth due to insufficient  
191 collision-coalescence of warm rain, which may favor large footprints of  $K_{DP}$  columns compared  
192 to  $Z_{DR}$  columns. A higher correlation between  $K_{DP}$  columns and total lightning flash rates would  
193 then suggest a significantly larger contribution of cold cloud processes to ice particle growth and  
194 storm electrification. In contrast, storms characterized by faster updrafts and substantial warm  
195 cloud depth may favor wider  $Z_{DR}$  column footprints (with considerable offset from  $K_{DP}$  columns)  
196 and a higher contribution of warm rain processes in the growth of graupel (Gupta et al. 2023).  
197 Subsequent noninductive charge separation between graupel and ice may eventually result in a  
198 greater correlation between  $Z_{DR}$  column volume and total lightning flash rates.

199 Past observational studies have aimed to develop single-parameter flash rate parameterization  
200 schemes in order to simulate lightning in numerical models, while examining the correlation  
201 between mixed-phase updraft kinematics (between -5° and -40°C isotherms), microphysics, and  
202 total lightning flash rates (Petersen et al. 2005a; Deierling et al. 2008; Deierling and Petersen  
203 2008; Basarab et al. 2015). However, the majority of these studies have relied on multi-Doppler  
204 radar analysis to estimate the vertical velocity and the volume of the updrafts. In their analysis  
205 of thunderstorms in the High Plains and northern Alabama, Deierling and Petersen (2008) found  
206 a strong correlation between total lightning flash rates and updraft volume (Pearson's correlation  
207 coefficient,  $r = 0.93$ ). In contrast, the correlation between flash rates and the mean and maximum

updraft speeds was lower ( $r < 0.8$ ). These findings were corroborated for thunderstorms in northern Alabama (Schultz et al. 2015), for a tornadic supercell in Oklahoma (Calhoun et al. 2014), and for a tornadic supercell in Kansas (Wiens et al. 2005). Across all these studies, the flash rates consistently exhibited a higher positive correlation with the updraft volume throughout the storm life cycle, as opposed to peak updraft velocity. However, Carey and Rutledge (1996) found the strongest correlation between flash rate and radar-implied graupel volume for a multi-cell storm in Colorado, while Basarab et al. (2015) found that updraft intensity measures like updraft volume or peak updraft speeds are less reliable predictors for total flash rate than graupel echo volume or 35 dBZ echo volume in the mixed-phase region for a small subset of thunderstorms in Colorado. Carey et al. (2019) attributed conflicting results in prior studies to the limited sample size of storms analyzed. To address this issue, they examined 33 independent storms in northern Alabama, encompassing a wide spectrum of convective modes and lightning flash rates. Even though they observed an overall decrease in the correlation between flash rate and storm kinematical and microphysical parameters, maximum updraft speed still had the weakest correlation with total flash rate ( $r = 0.6$ ), while graupel mass and volume exhibited the strongest correlation ( $0.69 \leq r \leq 0.76$ ). The authors concluded that radar-derived microphysical parameters are generally better correlated with total flash rate.

The goal of this study is to quantify the correlation between  $Z_{DR}$  and  $K_{DP}$  column volume (representative of mixed-phase microphysics as well as updraft volume and strength) and total lightning flash rates. These variables are interlinked through a complex feedback cycle involving dynamical, thermodynamical, and microphysical processes, as illustrated in Fig. 1. The temporal evolution of  $Z_{DR}$  columns in severe storms has been extensively studied in environments characterized by high instability and vertical wind shear (Picca 2010; Snyder et al. 2015; Kuster et al. 2019, 2020; Sharma et al. 2021). However, nonclassic tornadic storms in the high shear environments of the southeast USA lack a systematic investigation. Assuming that robust and wide updrafts lead to deeper and wider  $Z_{DR}$  and  $K_{DP}$  columns (Scharfenberg et al. 2005; Picca 2010; Homeyer and Kumjian 2015; Snyder et al. 2017), an increase in the volume of  $Z_{DR}$  and  $K_{DP}$  columns would correspond to a higher vertical mass flux within the mixed-phase region, resulting in enhanced precipitation and nonprecipitation ice mass flux. Increased ice mass flux would, in turn, suggest an increase in total flash rate. We hypothesize that the temporal fluctuations in the  $Z_{DR}$  and  $K_{DP}$

238 column volume correlate with the total lightning flash rates. Therefore, temporal trends in the  $Z_{DR}$   
 239 and  $K_{DP}$  column volume should capture the variability in total lightning flash rate through mod-  
 240 ulation of ice hydrometeor growth and subsequent noninductive charge separation (and lightning  
 241 initiation) under varying degrees of updraft intensity.



242 FIG. 1. Conceptual schematic highlighting the pathways that contribute to the complex feedback between  
 243 the dynamical, microphysical, and thermodynamical processes. Macro-scale storm characteristics such as the  
 244 updraft strength and lightning flash rates are modulated in part by these interlinked processes.

245    **2. Case description**

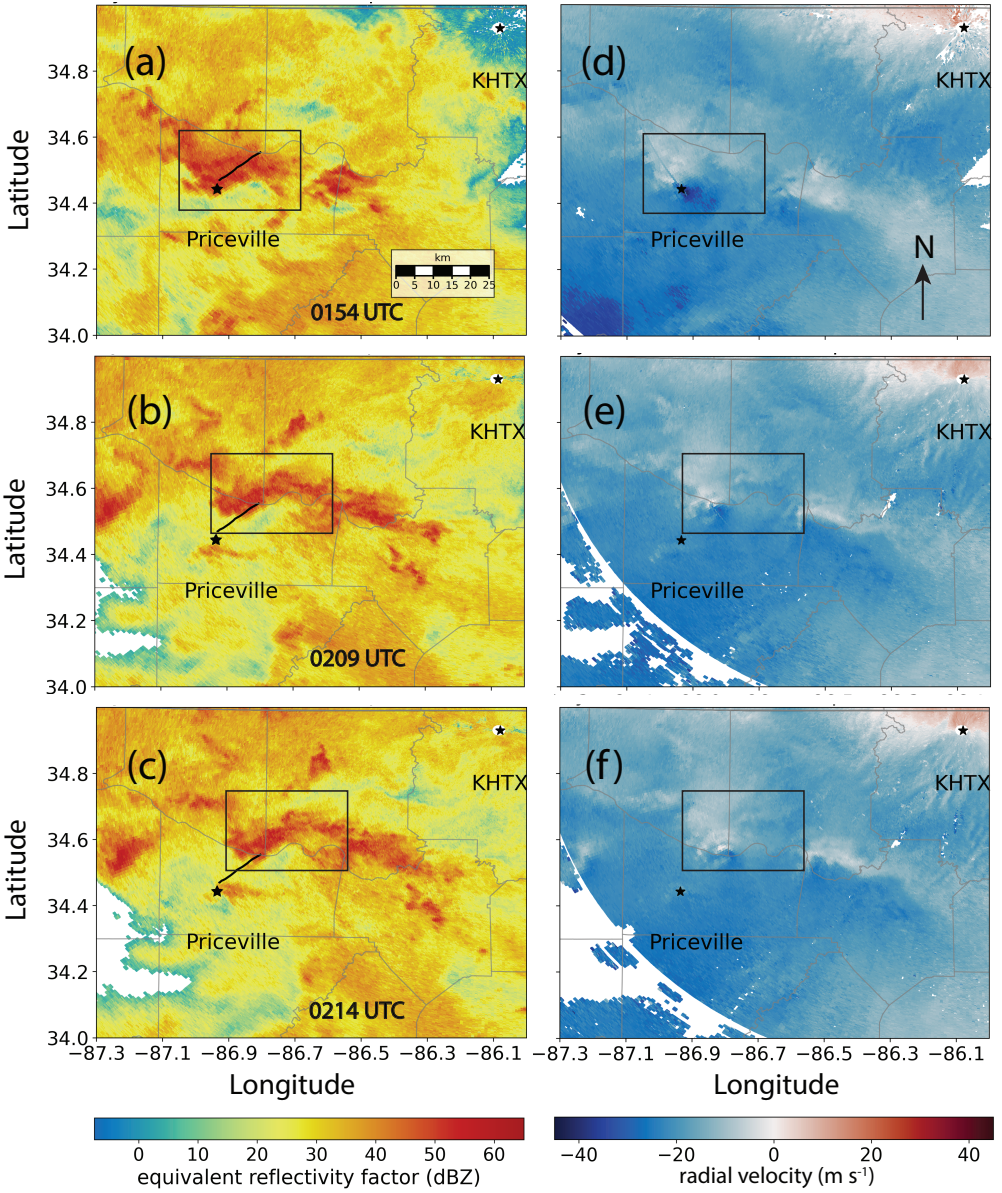
246    The field observing campaign of the VORTEX-SE project began in the spring of 2016 as an  
247    effort to understand the evolution of instability and boundary layer growth as large-scale weather  
248    systems passed over the southeastern United States. In this study, we analyze and compare the  
249    relationship between the total lightning flash rate and the volume of  $Z_{DR}$  and  $K_{DP}$  columns for  
250    potentially tornadic severe storms during three intensive observation periods (IOPs) of the 2016-17  
251    VSE field campaign. Below we provide a brief summary of each IOP. The bulk environmental  
252    parameters from the nearest sounding in space and time for each case are summarized in Table 1.  
253    A detailed description of the synoptic and mesoscale environment during for all three IOPs can be  
254    found in section S1 of the supplementary information.

255    *a. Tornadic supercell on 1 April 2016 (Case 1)*

256    During the late afternoon and evening hours on 31 March 2016, a hybrid multicell-supercell  
257    thunderstorm complex associated with a slow-moving cold front impacted the Tennessee Valley  
258    region. A supercell embedded within a large region of stratiform precipitation produced a tornado  
259    with a damage rating of 2 on the EF-Scale (McDonald and Mehta 2004) around 0154 UTC on  
260    1 April 2016 (Fig. 2). The tornado track was 15 km long and 183 m across at its widest point.  
261    The track began 4.8 km north of Priceville, Alabama, and terminated 3.2 km west of Bluff City,  
262    Alabama, around 0212 UTC (NCEI report 2016). The preconvective environment was favorable  
263    for organized convection, with a mixed-layer CAPE (ML CAPE) value of  $1118 \text{ J kg}^{-1}$  and 0–6 km  
264    bulk wind difference (BWD) in excess of  $28 \text{ m s}^{-1}$  (Fig. S3).

TABLE 1. Near-storm environmental parameters derived from radiosonde data representative of each case  
 analyzed in this study. SB refers to the surface-based parcel, ML refers to mixed-layer parcel representative of  
 the average potential temperature and mixing ratio in the lowest 100 hPa of the sounding, and EIL stands for  
 effective inflow layer.

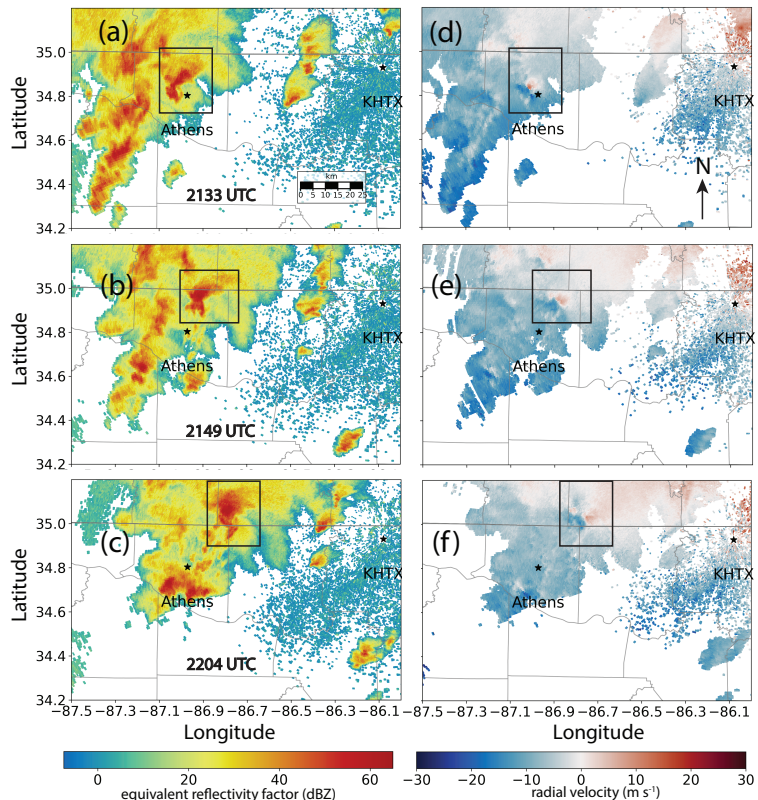
Environmental parameter	1 April 2016 (Case 1)	30 April 2016 (Case 2)	5 April 2017 (Case 3)
SB CAPE	$657 \text{ J kg}^{-1}$	$766 \text{ J kg}^{-1}$	$2265 \text{ J kg}^{-1}$
ML CAPE	$1118 \text{ J kg}^{-1}$	$663 \text{ J kg}^{-1}$	$1329 \text{ J kg}^{-1}$
Total precipitable water	1.44 in	1.49 in	1.15 in
Depth of EIL	1850 m	1264 m	1796 m
sfc–1 km SRH	$330 \text{ m}^2 \text{ s}^{-2}$	$59 \text{ m}^2 \text{ s}^{-2}$	$242 \text{ m}^2 \text{ s}^{-2}$
sfc–3 km SRH	$413 \text{ m}^2 \text{ s}^{-2}$	$131 \text{ m}^2 \text{ s}^{-2}$	$314 \text{ m}^2 \text{ s}^{-2}$
EIL SRH	$349 \text{ m}^2 \text{ s}^{-2}$	$101 \text{ m}^2 \text{ s}^{-2}$	$284 \text{ m}^2 \text{ s}^{-2}$
sfc–1 km BWD	$14 \text{ m s}^{-1}$	$8 \text{ m s}^{-1}$	$14 \text{ m s}^{-1}$
sfc–3 km BWD	$23 \text{ m s}^{-1}$	$20 \text{ m s}^{-1}$	$31 \text{ m s}^{-1}$
EIL BWD	$16 \text{ m s}^{-1}$	$13 \text{ m s}^{-1}$	$23 \text{ m s}^{-1}$
sfc–6 km BWD	$28 \text{ m s}^{-1}$	$24 \text{ m s}^{-1}$	$41 \text{ m s}^{-1}$



269 FIG. 2. Equivalent radar reflectivity factor (a-c; in dBZ), and radial velocity (d-f; in  $\text{m s}^{-1}$ ) from KHTX on  
 270 1 April 2016. The time period (0154–0214 UTC) depicted in these plots corresponds to the duration of the  
 271 Priceville, Alabama tornado. The boundaries of the tornadic supercell and the tornado track are indicated by  
 272 the rectangular box and the black line inside, respectively. Blue circles, green circles, and red triangles indicate  
 273 reports of severe wind, hail, and tornadoes within the preceding 30 minutes.

274 *b. Nontornadic supercell on 30 April 2016 (Case 2)*

275 A supercell at the leading edge of a multicell cluster in northern Alabama moved north-northeast  
 276 into southern TN between 2100 and 2200 UTC (Fig. 3). Limited ML CAPE and 0–1 km BWD  
 277 ( $663 \text{ J kg}^{-1}$  and  $7.7 \text{ m s}^{-1}$ , respectively) were not conducive for tornadic supercells, as revealed  
 278 by the 2000 UTC sounding near Moulton, Alabama (refer Fig. S6 for values of environmental  
 279 parameters). Additionally, effective inflow layer storm-relative helicity (SRH) and shear were  
 280 modest ( $\sim 101 \text{ m}^2 \text{ s}^{-2}$  and  $12.8 \text{ m s}^{-1}$ , respectively), indicating favorable conditions for potentially  
 281 disorganized multicell storms. Despite the observed intensification of low-level circulation near  
 282 Athens, Alabama around 2133 UTC on KHTX radar, the target supercell did not produce a tornado.



283 FIG. 3. Same as Fig. 2, but for the nontornadic supercell between 2133 and 2204 UTC on 30 April 2016. The  
 284 time period depicted in these plots corresponds to the instances of enhanced low-level rotation. The thick gray  
 285 line at  $35^\circ\text{N}$  latitude represents the Alabama-Tennessee border.

<sup>286</sup> c. Briefly tornadic supercell embedded in a QLCS on 5 April 2017 (Case 3)

<sup>287</sup> On 5 April 2017, Alabama experienced two rounds of severe storms. The first round occurred  
<sup>288</sup> between 0800 and 1400 UTC when elevated supercells, accompanied by damaging straight-line  
<sup>289</sup> winds and large hail, developed within the warm sector of a surface cyclone centered on the  
<sup>290</sup> Missouri-Illinois border. As the attendant warm front advanced northward and cloud cover de-  
<sup>291</sup> creased, direct insolation and near-surface moisture advection contributed to CAPE recovery over  
<sup>292</sup> the VSE domain. During the afternoon and evening, a southwesterly low-level jet formed ahead of  
<sup>293</sup> the cold front and continued eastward, advecting Gulf moisture into central and eastern Alabama.  
<sup>294</sup> The target storm originated in an environment characterized by an ML CAPE value of  $1329 \text{ J kg}^{-1}$   
<sup>295</sup> and 0–6 km BWD exceeding  $40 \text{ m s}^{-1}$ . During its initial stage, the target storm remained isolated  
<sup>296</sup> near the Sand Mountain plateau in northeastern Alabama, but later became embedded within a  
<sup>297</sup> rapidly developing QLCS (Fig. 4). Unofficial damage survey conducted by The University of  
<sup>298</sup> Alabama in Huntsville (UAH) confirmed a very narrow tornado damage track between 0003 and  
<sup>299</sup> 0006 UTC on 6 April 2017 near the Alabama-Tennessee border (VSE report 2017).

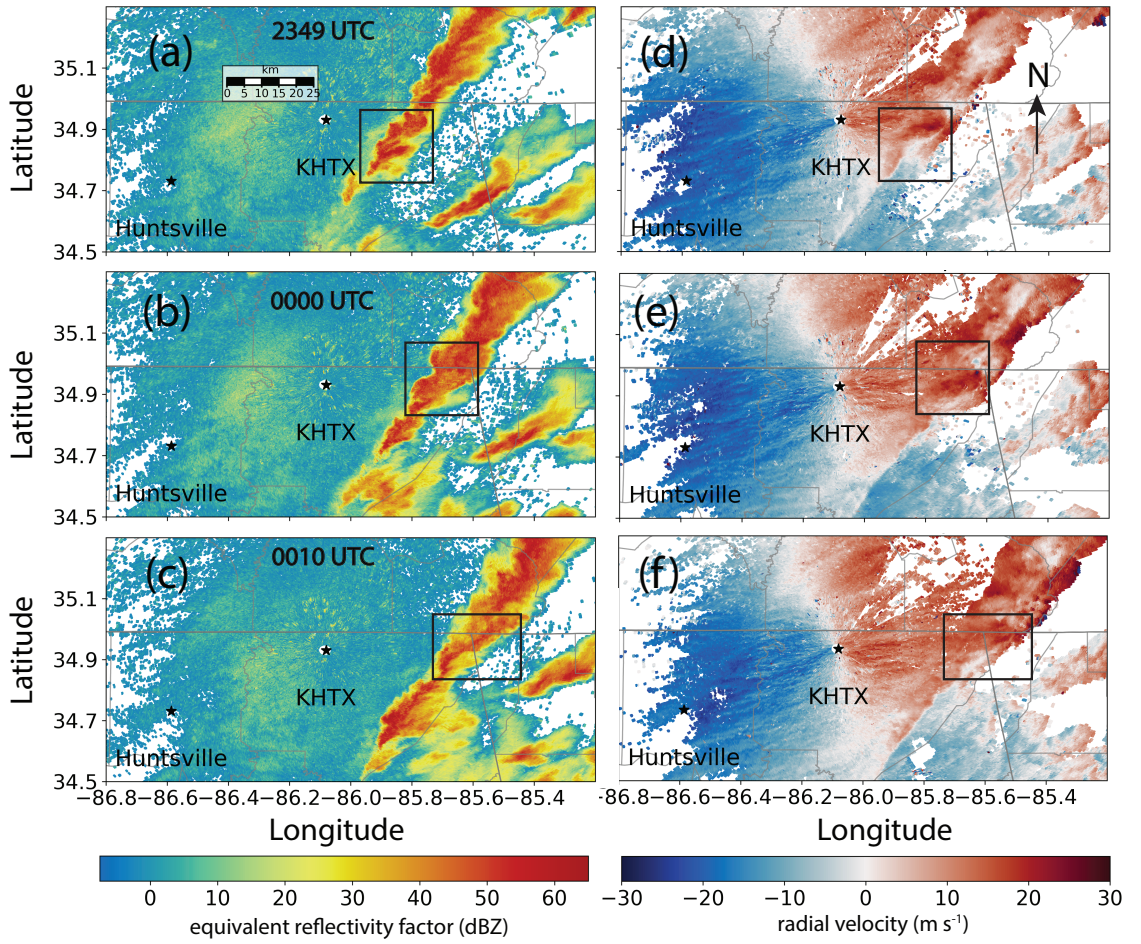


FIG. 4. Same as Fig. 2, but valid for a briefly tornadic supercell embedded in a QLCS between 2349 UTC 5 April 2017 and 0010 UTC 6 April 2017.

302 **3. Data and methodology**

303 *a. Instrumentation details*

304 **1) RADAR DATA:**

305 Microphysical evolution of the storms was analyzed using NEXRAD level-II (NOAA, National  
306 Centers for Environmental Information 2022) dual-polarization base data, including  $Z_{DR}$ ,  $\rho_{hv}$ , and  
307 total differential phase ( $\Phi_{DP}$ ). Polarimetric data from the UAH Advanced Radar for Meteorological  
308 and Operational Research (ARMOR; Petersen et al. 2005b) supplemented the WSR-88D data,  
309 providing observations of  $K_{DP}$  columns at a finer temporal resolution. The KHTX WSR-88D,  
310 with an antenna elevation of 566 m MSL, is located in Hytop, Alabama, and operated in VCP  
311 mode 212 during all three IOPs. The UAH ARMOR, with an antenna elevation of 206 m MSL,  
312 is situated at the Huntsville International Airport in Huntsville, Alabama. ARMOR operates at  
313 C-band frequency of 5625 MHz (~5 cm wavelength) and has a half-power beamwidth of 1.1°.  
314 Details regarding  $Z_{DR}$  and  $K_{DP}$  column processing from KHTX and ARMOR data can be found  
315 in section 3b1.

316 **2) LIGHTNING MAPPING ARRAY (LMA)**

317 Lightning data from the NASA North Alabama Lightning Mapping Array (NALMA; Koshak  
318 et al. 2004), supplemented by additional deployable stations from Texas Tech University (TTU;  
319 Carey and Stough 2017) were used for flash sort analysis and storm flash rate calculation (see section  
320 3b2 for details). The first step towards three-dimensional mapping of lightning flashes involves  
321 spatiotemporal clustering of very high frequency (VHF) sources emitted by stepped leaders during  
322 propagation of lightning channels (Rison et al. 1999; MacGorman et al. 2008). The VHF source  
323 location in space and time is calculated using the time of arrival method (Proctor 1971; Proctor et al.  
324 1988), and the accuracy of source location depends on factors such as the uncertainty associated  
325 with arrival time measurements and station network configuration (Koshak et al. 2004; Thomas  
326 et al. 2004; Chmielewski and Bruning 2016; Weiss et al. 2018). Like any inverse problem in  
327 geophysics, uncertainties exist in the determination of source locations. Through the application of  
328 geometric and theoretical models, Thomas et al. (2004) and Koshak et al. (2004) found that small  
329 errors in source arrival times can result in large errors in the estimation of source altitude. While

azimuthal errors increase linearly with range, range and altitude errors can grow proportionally to the square of the range. Therefore, it is important to characterize the range dependence of detection efficiency and errors in source azimuth and altitude (Fuchs et al. 2016; Chmielewski and Bruning 2016; Weiss et al. 2018). With 14 active stations during the three IOPs, NALMA detected at least 95% of flashes within a 100-km radius encompassing the region where the three severe storms occurred (refer Fig. S9a). The source detection efficiency within this region exceeded 90%, with an average error in VHF source altitude of less than 100 m (refer Figs. S9a and b).

### 3) NATIONAL LIGHTNING DETECTION NETWORK (NLDN)

Examining the timing and polarity of cloud-to-ground (CG) flashes can reveal crucial information about the precipitation processes and electrical structure of a storm (Boccippio et al. 2001; MacGorman et al. 2011). CG stroke and IC pulse data were obtained from the U.S. National Lightning Detection Network (NLDN), which operates wideband sensors (400 Hz to 400 kHz; Orville 2008). While ground-based lightning location systems like the NLDN have a high detection efficiency for CG flashes, reaching up to 95% (Mallick et al. 2014), these systems tend to be less efficient at detecting intra-cloud (IC) lightning flashes (Murphy et al. 2021). The NLDN flash clustering algorithm described in section 3a of Murphy et al. (2021) was used to group CG strokes and IC pulses into CG flashes.

#### *b. Observational analysis methods*

##### 1) $Z_{DR}$ AND $K_{DP}$ COLUMN PROCESSING

KHTX data were used for  $Z_{DR}$  column analysis in all cases due to the reduced susceptibility of WSR-88D to  $Z_{DR}$  calibration errors and a lower resonance (non-Rayleigh) scattering effect at S-band wavelength. We intended to use the  $K_{DP}$  field from ARMOR data for all cases, which was calculated using the iterative filtering approach proposed by Hubbert and Bringi (1995) and included by default in the processed ARMOR data files. However, for Case 3 (5 April 2017), when the target storm extended beyond the maximum scan range of ARMOR, we had to compute the  $K_{DP}$  field using NEXRAD level-II data. For this purpose, the KHTX total differential phase field was used to retrieve the  $K_{DP}$  values using the linear programming (LP) phase processing function in Py-ART (Giangrande et al. 2013). The specific parameters used in the  $K_{DP}$  processing algorithm

can be found in Table 4. Upon comparing the  $K_{DP}$  field output from the LP phase processing algorithm (for KHTX) and the Hubbert and Bringi (1995) method (ARMOR) for Cases 1 and 2 (not shown), we found the differences in the areal extent of the  $1 \text{ deg km}^{-1}$  contour were not substantial enough to alter the qualitative interpretation of our results. This finding justified our use of the  $K_{DP}$  field from KHTX data for our analysis in Case 3.

Objective analysis was performed on ARMOR and KHTX radar scan volumes from the native spherical coordinate system to a three-dimensional Cartesian grid. The gridding process used a single-pass, distance-dependent weighted-average Barnes filter (Barnes 1964; Koch et al. 1983; Majcen et al. 2008). Prior to gridding, nonmeteorological echoes and other small, disjoint artifacts in each volume scan were removed using the despeckling operation in Py-ART (Helmus and Collis 2016). Additionally, range gates were masked out when  $Z_{DR}$  values fell outside the range of [-2, 6] dB,  $\rho_{hv}$  values were below 0.95, or Z values dropped below 20 dBZ, as per Ryzhkov and Zrnic (1998). The Cartesian grid had a horizontal and vertical spacing of 500 m, facilitating volumetric analysis of  $Z_{DR}$  and  $K_{DP}$  columns. The dimensions of the overall grid size were selected such that storm features were optimally resolved, as outlined in Table 2. Notably, a different grid size (with the same 500 m spacing for all three dimensions) was used when calculating the  $K_{DP}$  column volume from ARMOR. See Table 3 for further details.

Finally, an improved version of Chernyaev's Marching Cubes algorithm (Chernyaev 1995; Lewiner et al. 2003) was employed to identify the  $Z_{DR}$  and  $K_{DP}$  column objects in the gridded volume. The Marching Cubes algorithm iterates across the volume, searching for regions with values exceeding a user-defined threshold. Upon identifying such a region, triangulations are generated and added to an output mesh, resulting in a collection of vertices and triangular faces. We utilized the version of the algorithm provided with the ‘scikit-image’ Python package (van der Walt et al. 2014) to identify the regions with  $Z_{DR} \geq 1 \text{ dB}$  and  $K_{DP} \geq 1 \text{ deg km}^{-1}$  above the environmental  $0^\circ\text{C}$  level. Several past studies have used these threshold values for identifying the cores of  $Z_{DR}$  and  $K_{DP}$  columns (Snyder et al. 2015; Kuster et al. 2020; Krause and Klaus 2024). A manual inspection was carried out to verify that only column objects belonging to the target storm were included in the object volume calculation. This step was necessary to eliminate any potential inclusion of column objects from surrounding convection within the grid. The time series of  $Z_{DR}$  and  $K_{DP}$  column volumes was then obtained by aggregating the volumes of all mesh objects

388 present at a given time. If multiple mesh objects were detected, their volumes were summed up to  
389 calculate the total column volume.

390 TABLE 2. Details of the overall grid size used to analyze  $Z_{DR}$  and  $K_{DP}$  columns using KHTX data. The grid  
391 spacing in all three directions ( $\Delta x = \Delta y = \Delta z$ ) was 500 m. Grid origin was set to KHTX coordinates.

IOP	Storm mode	Grid size (x,y,z)	Grid bounding box (min lon , min lat , max lon , max lat )
1 April 2016	Tornadic supercell	120 km × 90 km × 15 km	(-87.62, 34.02, -86.30, 34.84)
30 April 2016	Nontornadic supercell	110 km × 95 km × 15 km	(-87.62, 34.34, -86.41, 35.19)
5 April 2017	Supercell embedded within QLCS	110 km × 120 km × 15 km	(-86.30, 34.57, -85.09, 35.65)

392 TABLE 3. Details of the overall grid size used to analyze  $K_{DP}$  columns in the tornadic (Case 1) and nontornadic  
393 (Case 2) supercells using ARMOR data. The grid spacing in all three directions ( $\Delta x = \Delta y = \Delta z$ ) was 500 m.  
394 Grid origin was set to ARMOR coordinates.

IOP	Storm mode	Grid size (x,y,z)	Grid bounding box (min lon , min lat , max lon , max lat )
1 April 2016	Tornadic supercell	120 km × 80 km × 15 km	(-87.65, 34.10, -86.33, 34.82)
30 April 2016	Nontornadic supercell	75 km × 90 km × 15 km	(-87.16, 34.56, -86.33, 35.36)

395 TABLE 4. Parameters used for retrieval of  $K_{DP}$  field from KHTX differential phase data using the LP phase  
 396 processing method in the Py-ART function ‘pyart.correct.phase\_proc\_lp’.

Parameter name	Parameter definition	Parameter value
offset	Reflectivity offset in dBZ	0
self_const	Self consistency factor	60000
low_z	Low limit for reflectivity: reflectivity < low_z set to low_z	10
high_z	High limit for reflectivity: reflectivity < high_z set to high_z	53
min_phidp	Minimum differential phase	0.01
min_ncp	Minimum normal coherent power	0.5
min_rhv	Minimum copolar coefficient	0.8
fzl	Level of environmental freezing level	3600
window_len	Length of Sobel window applied to $\Phi_{DP}$ prior to calculating $K_{DP}$	35
coef	Exponent linking Z to $K_{DP}$ in self consistency	0.914

397 2) FLASH SORTING AND CLUSTERING TO GENERATE GRIDDED FLASH PRODUCTS

398 Level 1B LMA data contains geolocated coordinates (x, y, z, and t) of each VHF source  
399 detected by the station network. The first order processing of the LMA data involved sorting and  
400 clustering these VHF sources into individual lightning flashes (Fuchs et al. 2016; Chmielewski et al.  
401 2022). The flash sorting and clustering process involved grouping the VHF sources into flashes  
402 using the Density-Based Spatial Clustering of Applications with Noise algorithm (DBSCAN;  
403 Ester et al. 1996), as implemented in the ‘lmatools’ software (Bruning 2015, downloaded from  
404 <https://github.com/deeplycloudy/lmatools>). The grouping operation was performed after filtering  
405 out noise sources with a reduced chi-square ( $\chi^2_v$ ) value  $> 1$  [based on a 80-ns timing error for  
406 six NALMA stations, as in Thomas et al. (2004)]. A cluster of VHF sources was classified as  
407 a lightning flash if it met the following criteria: it contained 10 or more sources detected by at  
408 least six ground stations, and all sources comprising the flash occurred within a 3 km distance and  
409 150-ms time interval from the first source belonging to that flash (MacGorman et al. 2008; Bruning  
410 and MacGorman 2013), with a maximum flash duration of 3 s.

411 3) TIME-HEIGHT ANALYSIS OF POLARIMETRIC VARIABLES

412 Vertical profiles of polarimetric radar variables provide insights into the life cycle of deep  
413 convective updrafts. The vertical profiles can help elucidate the temporal evolution of mixed-phase  
414 microphysical processes in the updraft core and the subsequent precipitation fallout. Descending  
415 precipitation shafts are often characterized by vertical size sorting of hydrometeors, with a gradual  
416 progression of high  $Z_{DR}$  values towards the surface. The size sorting of raindrops can persist when  
417 storm-relative winds are present, or when other processes such as evaporation alter the drop size  
418 distribution during precipitation descent. Therefore, the sedimentation of large raindrops, graupel,  
419 or wet hailstones can transport charge layers to lower levels. This process influences the altitude  
420 of flash initiation and highlights the electrically active regions within a thunderstorm, ultimately  
421 determining the polarity of cloud-to-ground flashes.

422 To ensure a consistent radar resolution across all polarimetric variables, we exclusively used  
423 gridded polarimetric data from the KHTX radar. The time-height cross-sections were generated  
424 by extracting the polarimetric variables at the location of peak reflectivity for each vertical level.  
425 In order to exclude contribution from neighboring thunderstorms within the multicell complex,

a two-step procedure was employed. Firstly, storm cells across the entire domain were tracked based on a 40-dBZ threshold in the gridded reflectivity field at 1 km ARL using the ‘tobac’ Python package (Heikenfeld et al. 2019). Then, a search mask was created to restrict the search range to a 12-km radius around the centroid of the 40-dBZ reflectivity field identified in the previous step, for each radar scan. Within this search radius, the maximum reflectivity value and its corresponding location were extracted at each time and vertical level throughout the grid. Once the coordinates of the maximum reflectivity were determined, the value of other polarimetric variables were calculated at the same (x, y) location for each vertical level and analysis time. To create the VHF source density cross-sections, the source density (count of the VHF sources on the same grid as polarimetric data) was horizontally integrated for the duration of each radar volume scan. The VHF source density from nearby thunderstorms was excluded using a manual polygon boundary around the target storm. The low-level reflectivity and two-dimensional planar projection of VHF source density were used as guides to isolate the target storm.

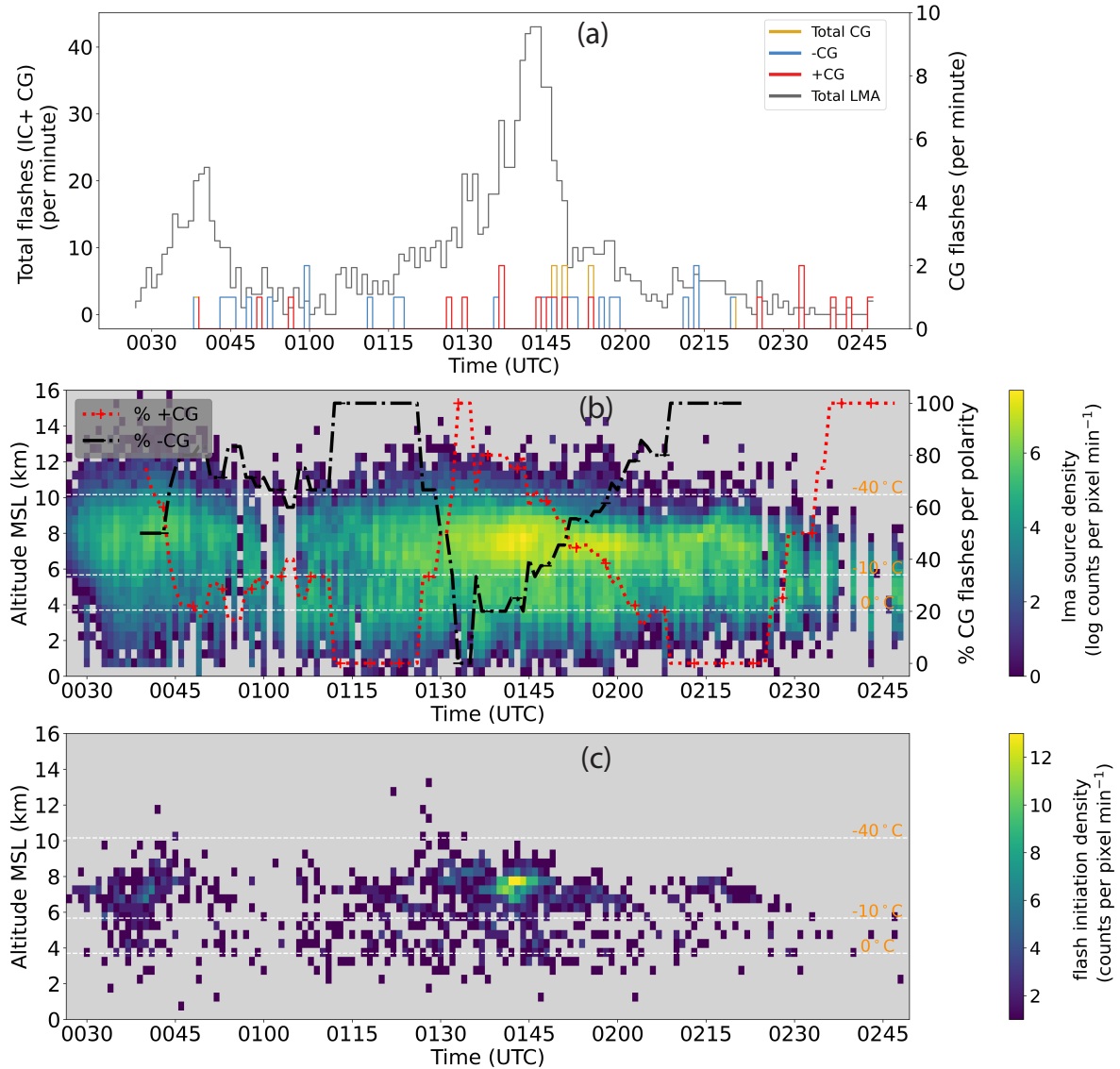
## 4. Results and discussion

### a. Lightning data analysis

#### 1) CHARACTERIZING FLASH RATES, POLARITY, AND TIME-HEIGHT VARIATION OF LIGHTNING FLASHES

(i) *Case 1 (1 April 2016)*: The tornadic supercell exhibited a peak LMA total flash rate of 22 flashes  $\text{min}^{-1}$  at 0040 UTC, which then nearly doubled to 43 flashes  $\text{min}^{-1}$  an hour later at 0142 UTC (Fig. 5a). During the first peak in total flash rate, most lightning flashes initiated and propagated between 6 and 10 km MSL (or -10° to -40°C layer; Fig. 5b and c). At least 80–90% of the CG flashes during this period had a negative polarity. The second peak in total flash rate from 0135 to 0150 UTC was accompanied by a three-fold increase in both source density and flash initiation density (FID) around 8 km MSL, within the mixed-phase region (Fig. 5b and c). The peak CG flash rate did not exceed 2 flashes  $\text{min}^{-1}$  throughout the analysis period. There were a couple of instances between 0055 and 0105 UTC when the CG flash rate was either comparable to or slightly higher than the LMA total flash rate. This discrepancy in LMA total flash rate and NLDN CG flash rate is likely due to a combination of issues with the NLDN CG classification and flash clustering algorithms. For instance, between 0100 and 0101 UTC, NLDN reported eight -CG strokes that were clustered into two CG flashes, whereas NALMA detected only one flash.

455 LMA observations during this period confirmed that all these return strokes belonged to the same  
456 parent flash (not shown). At other times, NLDN can misclassify strong K-changes and inverted  
457 IC flashes as -CG flashes resulting in an overestimated CG flash rate (Murphy et al. 2021). The  
458 increased +CG flash rate just before tornadogenesis at 0154 UTC is similar to the tendency of  
459 storms over the Great Plains to produce tornadoes shortly after attaining their peak +CG flash  
460 rate (Curran and Rust 1992; MacGorman and Burgess 1994; Bluestein and MacGorman 1998;  
461 Carey and Rutledge 1998). Unfortunately, there is a lack of research on this phenomenon for  
462 storms in the southeast U.S. Further investigation with a larger sample size is needed to establish a  
463 more definitive understanding of the relationship between +CG flashes and tornadogenesis in the  
464 southeast United States.



465 FIG. 5. (a) Total flash rate (from NALMA) and CG flash rate (from NLDN) at 1 minute interval within the  
 466 Priceville supercell on 1 April 2016. +CG, -CG, and total CG flash rates are plotted in red, blue, and yellow  
 467 colors, respectively. CG flashes were filtered using a subjective threshold of  $\pm 15$  kA to exclude IC flashes  
 468 misclassified as CG flashes in the NLDN database. (b) Time–height variation of flash source density, and (c)  
 469 flash initiation density in the Priceville supercell as derived from gridded NALMA data (aggregated count per  
 470 minute). Black and red lines in (b) correspond to a 15 minute rolling mean of percentage of negative and positive  
 471 CG flashes out of total CG flashes, respectively.

*(ii) Case 2 (30 April 2016):* The nontornadic supercell had a significantly greater peak total flash rate of 108 flashes  $\text{min}^{-1}$  (at 2219 UTC) compared to the tornadic supercell (Fig. 6a). However, the peak CG flash rate for the nontornadic supercell was slightly larger (4–5 flashes  $\text{min}^{-1}$ ). Unlike the tornadic storm, the peak CG flash rate in the nontornadic storm occurred around the same time as the peak in total flash rate. All CG strikes during the first 90 minutes of the storm lifetime (2030–2140 UTC) lowered negative charge to the ground. The first +CG flash was observed at 2145 UTC, with such flashes being infrequent for the remainder of the analysis period. Notably, the majority of these +CG flashes occurred between 2200 and 2225 UTC, coinciding with a significant increase in the low-level VHF source density (cf. Fig. 8j). This finding suggests that the +CG strikes may have been associated with discharges between the mid- and low-level charge layers. The magnitude of VHF source density and FID in the lower ( $0^\circ$  to  $-10^\circ\text{C}$ ) and upper ( $-10^\circ$  to  $-40^\circ\text{C}$ ) charge dipoles was comparable until 2210 UTC (Fig. 6b and c). However, between 2210 and 2220 UTC, there was a sudden surge in flash initiations in both the lower and upper dipoles, referred to as a lightning jump, which contributed to the peak in the total flash rate. Until this time, -CG flash strikes were frequent and constituted over 80% of all CG flashes. A decrease in the overall flash initiation rate between 2245 and 2255 UTC coincided with a rapid decline in CG flashes. From 2300 UTC onwards, flash initiations were predominantly concentrated near the lower dipole ( $0^\circ$  to  $-10^\circ\text{C}$  layer), resulting in additional -CG strikes.

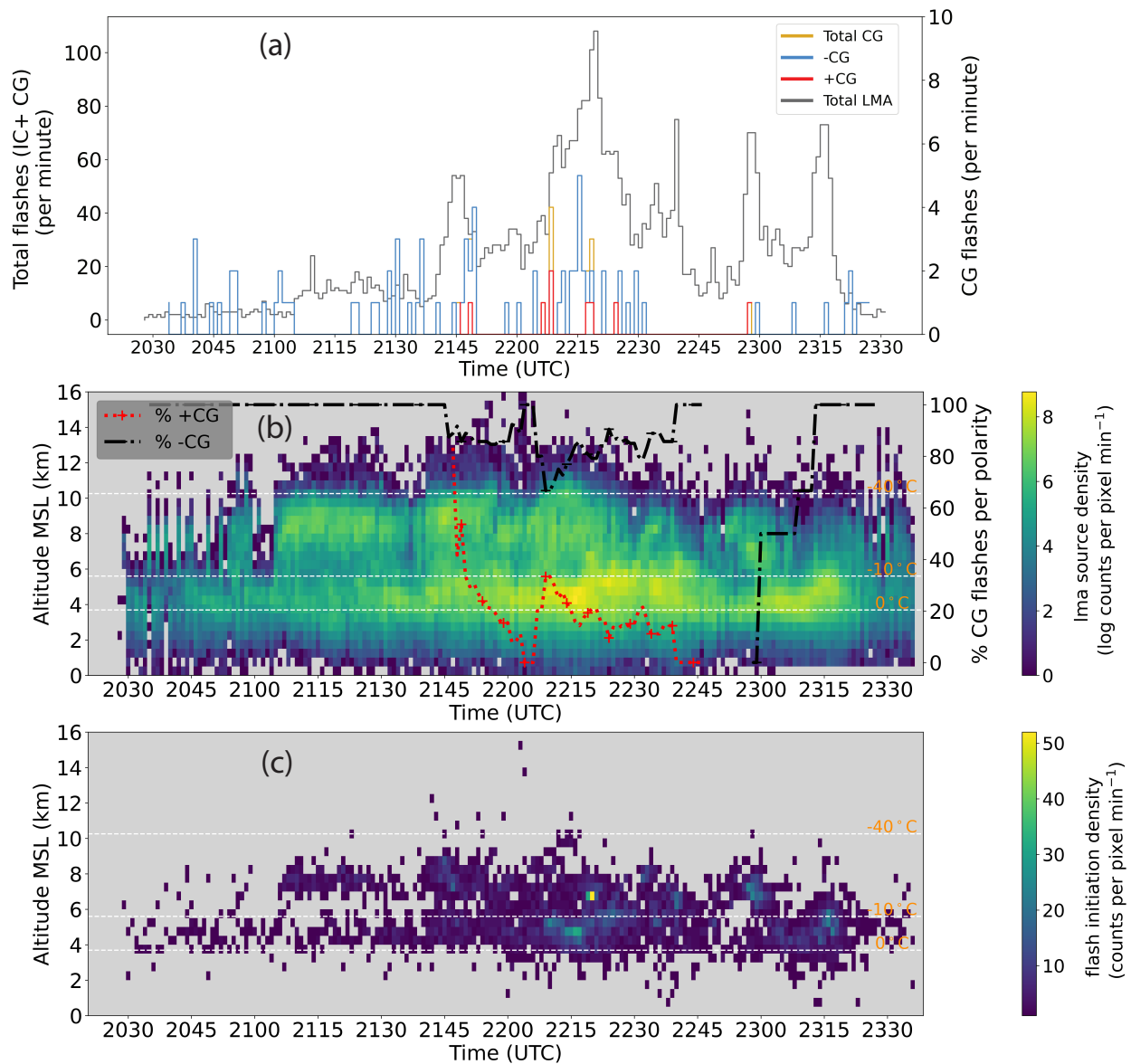


FIG. 6. Same as Fig. 5, except for the nontornadic supercell on 30 April 2016.

490 (iii) *Case 3 (5 April 2017):* Due to the challenges in isolating lightning flashes from the QLCS  
491 segment that contained the tornadic circulation, the analysis presented for this case is more sub-  
492 jective compared to the previous two quasi-isolated storms. To narrow down our analysis to the  
493 specific circulation that resulted in tornadogenesis around 0003 UTC on 6 April 2017, we used the  
494 local maximum in the KHTX low-level azimuthal shear field. By tracing this circulation back in  
495 time, we were able to determine its initial appearance at 2329 UTC on 5 April 2017. This approach  
496 allowed us to focus our analysis on the updrafts associated with the tornadic mesocyclone. The  
497 coordinates of the circulation were manually recorded to overcome the limitation of automated  
498 tracking methods to produce continuous storm tracks. The total flash rate increased monotonically  
499 between 2300 and 2350 UTC, reaching a peak value of more than 100 flashes  $\text{min}^{-1}$  (Fig. 7a). Fol-  
500 lowing this peak, the flash rate decreased to 40 flashes  $\text{min}^{-1}$  over the next 10 minutes. Throughout  
501 the analysis period, CG flashes had a predominantly negative polarity, with the peak CG flash rate  
502 of 7 flashes  $\text{min}^{-1}$  around 2358 UTC (Fig. 7a). The percentage of -CG flashes varied between 70  
503 and 100% throughout the analysis period (Fig. 7b). Unlike the previous two cases, the maximum  
504 VHF source density and FID in this storm occurred exclusively near the  $-40^\circ\text{C}$  level (or 9 km  
505 MSL). This clustering tendency also explains the relatively low fraction of +CG flashes, which did  
506 not exceed 40% at any point during the analysis period. Interestingly, the largest increase in the  
507 fraction of +CG flashes (and steepest decline in -CG flashes) around 2352 UTC occurred following  
508 a sharp cutoff in the source density at 9 km altitude, while the FID exhibited minimal change. This  
509 finding suggests the possibility of increased +CG flash strikes in the upshear or downshear anvil  
510 region of the QLCS (refer Fig. S15).

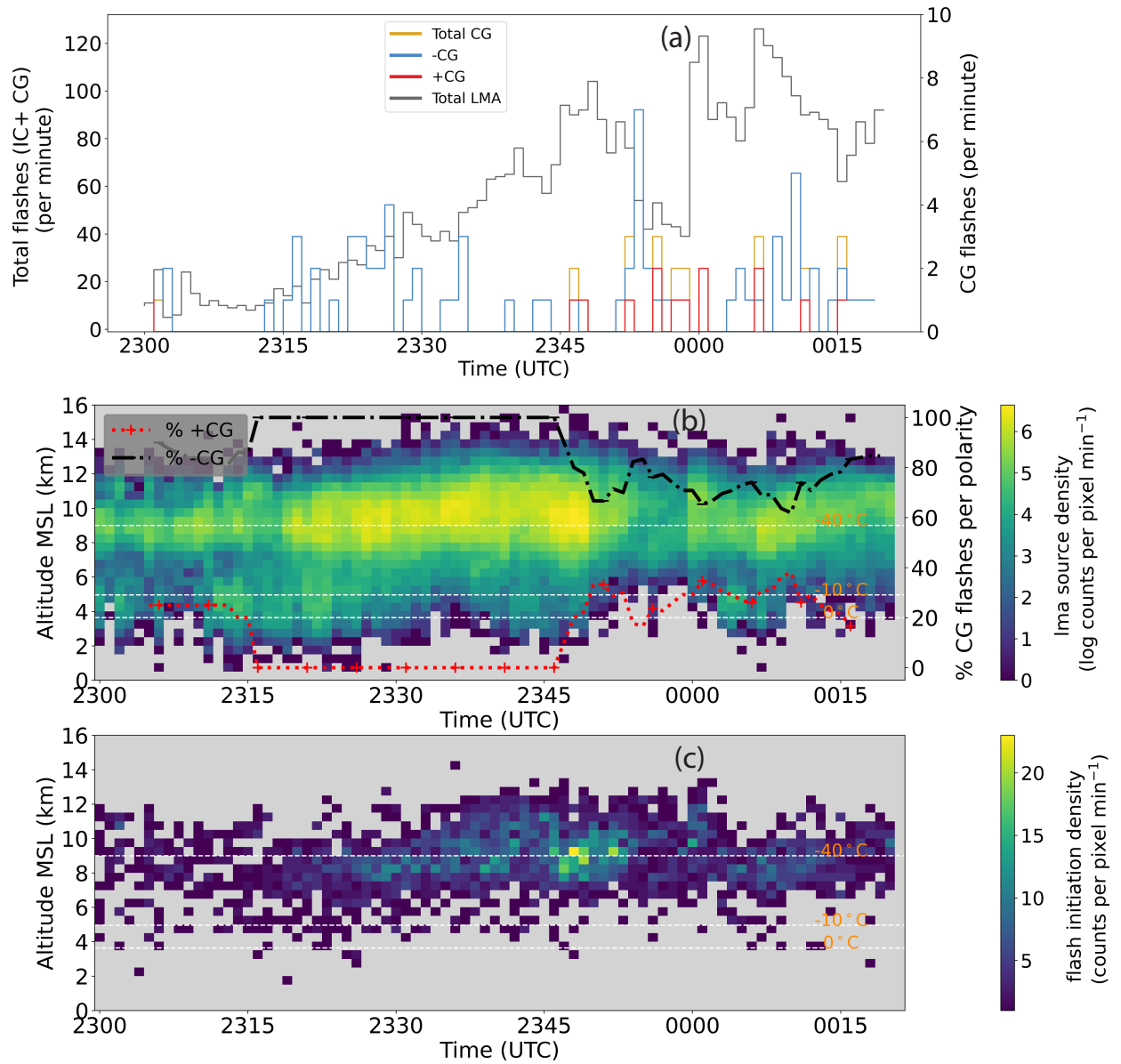


FIG. 7. Same as Fig. 5, except for the supercell embedded within the QLCS on 5 April 2017.

511    b. *Storm lifecycle and temporal trends in Z<sub>DR</sub> and K<sub>DP</sub> column volume, and lightning flash rates*

512    (i) *Case 1 (1 April 2016):* The tornadic supercell initiated approximately 160 km southwest of  
513    KHTX, where the lowest radar beam intercepted the reflectivity core at an altitude of  $\sim 4$  km above  
514    the radar level (ARL; not shown). The peak reflectivity values ( $> 65$  dBZ) reached an altitude  
515    of 6 km ARL between 0040 and 0055 UTC (Fig. 8a). During this period the 30-dBZ echo top  
516    height extended up to 10 km ARL. A noticeable reduction in the  $\rho_{hv}$  values ( $< 0.85$ ) between  
517    0030 and 0045 UTC in conjunction with large spectrum width ( $6\text{--}8 \text{ m s}^{-1}$ ) and noisy Z<sub>DR</sub> suggests  
518    contamination from three-body scatter spike and the presence of wet hail (Zrnić 1987; Emersic  
519    et al. 2011, refer Figs. 8c and S11). However, during this period, the storm was at its farthest  
520    distance from the KHGX radar, which may introduce more uncertainty in the gridded Z<sub>DR</sub> values.  
521    After 0115 UTC, the maximum reflectivity values did not exceed 60 dBZ and were predominantly  
522    found within the 2.5–5 km ARL layer. High reflectivity values descended to lower levels (between  
523    the surface and 1 km ARL) around 5–10 minutes later (denoted by black lines in Fig. 8a). As  
524    the storm reached its dissipation stage (post 0235 UTC), the 30-dBZ echo top height gradually  
525    decreased, extending only up to 7 km ARL.

526    There were several instances until 0220 UTC when enhanced Z<sub>DR</sub> values ( $\sim 2\text{--}3$  dB) extended up  
527    to 2 km above the environmental 0°C level ( $\sim 4$  km), indicating the presence of supercooled liquid  
528    water and wet hydrometeors. The descent of high Z<sub>DR</sub> values to lower levels around 10–15 minutes  
529    later (indicated by solid green lines in Fig. 8b around 0050, 0125, and 0210 UTC) suggests melting  
530    hailstones and large raindrops close to ground. Low values of correlation coefficient ( $< 0.95$ )  
531    along with higher Z<sub>DR</sub> values (1–3 dB) both above and below the 0°C level suggest the presence of  
532    mixed-phase precipitation and melting hailstones, respectively (Fig. 8c). The presence of a large  
533    concentration of raindrops and partially melted hailstones is further supported by high K<sub>DP</sub> values  
534    ( $\sim 2 \text{ deg km}^{-1}$ ) extending from 6 km ARL down to the surface post 0115 UTC (Fig. 8d). The  
535    highest VHF source density at upper levels (within the 6–8 km layer) was observed around 0135  
536    UTC, coinciding with the descent of high Z<sub>DR</sub> values to the surface (Fig. 8b and e). However,  
537    Z<sub>DR</sub>,  $\rho_{hv}$ , and K<sub>DP</sub> exhibited a relative minimum aloft (within the 3.5–6 km layer), indicating  
538    the presence of graupel, which is consistent with active electrification and observed lightning  
539    production (Fig. 8b-d). A bi-level maximum in VHF source density was centered around 4 km  
540    and 8 km MSL between 0115 and 0205 UTC (Fig. 8e). This coincided with the period of highest

total and CG flash rates (Fig. 5a), indicating that both the upper and lower charge dipoles were electrically active during this period. The  $Z_{DR}$  and  $K_{DP}$  column volume in the Priceville, Alabama tornadic supercell attained peak values during the first lightning jump at 0040 UTC, followed by a collapse around the time of the second lightning jump (0142 UTC), when the total flash rate was highest (Fig. 9a). In the 10 minutes leading up to tornadogenesis at 0154 UTC, the  $Z_{DR}$  column volume increased, followed by a subsequent decline. The sharp decrease in the  $K_{DP}$  column volume after 0154 UTC can be attributed to the storm entering ARMOR's cone of silence. This may have led to the potential updraft surge linked with the second lightning jump not being detected in the  $K_{DP}$  column volume. Despite the missing  $K_{DP}$  column volume data in the later stages of the storm life cycle, the overall total flash rate had a stronger correlation with the  $K_{DP}$  column volume ( $r = 0.54$ ) compared to  $Z_{DR}$  column volume ( $r = 0.37$ ). This finding aligns with previous research that has established a positive correlation between the  $K_{DP}$  column volume and updraft mass flux, a kinematic variable commonly employed to parameterize lightning flash rates in thunderstorms (Wiens et al. 2005; Deierling et al. 2008; van Lier-Walqui et al. 2016).

The  $Z_{DR}$  column volume increased monotonically with the total lightning flash rate until 0110 UTC (Fig. 9a). This trend suggests that the early stage of storm evolution was characterized by steady updrafts. These updrafts were likely strong enough for vertical size sorting of supercooled cloud condensate, while also providing the liquid water necessary for graupel growth and storm electrification. The erratic fluctuations in the  $Z_{DR}$  column volume post 0110 UTC could be due to the transition of updrafts to a non-steady state, resulting in low covariability between the  $Z_{DR}$  column volume and total lightning flash rate. A stronger correlation between the  $K_{DP}$  column volume and the total lightning flash rate between 0100 and 0210 UTC could be due to a more synchronized graupel production/sink and noninductive charging rates from cold cloud processes, such as partial melting of ice and/or riming of wet/mixed-phase hydrometeors during this period. There were also instances when the rapid increase in lightning flash rate was not captured by both  $Z_{DR}$  and  $K_{DP}$  column volume (second lightning jump at 0142 UTC; Fig. 9a). Most lightning flashes around the time of the second lightning jump occurred between the -20 and -30°C levels. However, both the  $Z_{DR}$  and  $K_{DP}$  column volumes showed a decreasing trend 10 minutes before the lightning jump. It is challenging to explain the delay between the peak  $K_{DP}$  column volume and lightning flash rates without *in situ* measurements. One possibility is that the ice crystals were too

571 small and/or the liquid water content (LWC) at higher altitudes was too low for efficient riming to  
572 produce enhanced  $K_{DP}$  values at the time of lightning jump (Waltz et al. 2022). Another possibility  
573 is that the slower, time-integrated growth of ice particles and strengthening of the electric field  
574 could have caused this apparent lag. Additionally, the optimal local eddy flow structure conducive  
575 for flash initiation might have occurred at a later time.

576 Overlaying the locations of lightning initiations (on a two-dimensional horizontal plane) with  
577 the  $Z_{DR}$  and  $K_{DP}$  column footprints at the 0°C level can provide valuable insights into the spatial  
578 orientation of electrically active regions relative to the storm updrafts. We observed a difference  
579 in the spatial orientation of the polarimetric fingerprints in relation to the location of flash activity.  
580 To quantitatively confirm this, we calculated the number of flash initiations within and outside  
581 the footprint of the  $K_{DP}$  and  $Z_{DR}$  columns at the 0°C level, along with their corresponding areas  
582 (Fig. 9b and c). The Priceville supercell had over 90% of total flashes initiating outside the  $Z_{DR}$   
583 column footprint. The mean flash area within the  $Z_{DR}$  column footprint was 18 km<sup>2</sup>, whereas  
584 flashes initiating outside the  $Z_{DR}$  column had a mean area of 53 km<sup>2</sup>. In contrast, approximately  
585 57% of total flashes initiated within the  $K_{DP}$  column footprint, with an average flash area of 17  
586 km<sup>2</sup>, compared to 30 km<sup>2</sup> for flashes initiating outside the  $K_{DP}$  column. This finding implies a  
587 disproportionate amount of flash initiations away from the main updraft core. This phenomenon  
588 may be attributed to the rapid downshear advection of charged hydrometeors, combined with the  
589 slower volume scans of WSR-88D compared to the fast storm motions observed in high-shear  
590 environments in the southeastern USA. It would be worthwhile to compare the  $Z_{DR}$  and  $K_{DP}$   
591 column footprints from a rapid-scan radar in order to validate the cause of this spatial offset.

592 (ii) *Case 2 (30 April 2016):* During the lifetime of the nontornadic supercell, three distinct  
593 updraft pulses around 2115, 2140, and 2215 UTC resulted in the 30-dBZ echo top height reaching  
594 an altitude of 10 km. Notably, the maximum reflectivity values remained constant at 60–65 dBZ  
595 throughout the analysis period (Fig. 8f). During the time period between 2105 and 2130 UTC,  
596 the presence of reduced  $Z_{DR}$  values throughout the depth of the precipitation shaft, along with  
597 relatively low values of  $\rho_{hv}$  and  $K_{DP}$ , suggested the likelihood of a hail shaft dominated by dry  
598 hail growth (Fig. 8g-i). In contrast, post 2135 UTC, there were noticeable enhancements in  $Z_{DR}$   
599 values ( $\geq 4$  dB), along with moderately high  $\rho_{hv}$  ( $\sim 0.95$ ) and relatively high values of  $K_{DP}$  (2–3  
600 deg km<sup>-1</sup>) at the mid-levels (3–5 km ARL). These observations indicate the presence of a mixture

of melting graupel/hail with rain (Fig. 8g-i). Throughout the analysis period, the VHF source density exhibited a bi-level maximum, centered around 4 and 9 km MSL. However, between 2205 and 2245 UTC, there was a significant increase in source density at lower levels, reaching down to 2 km MSL (Fig. 8j). Coinciding with this increase, the peak values of total and CG flash rates (100 and 7 flashes min<sup>-1</sup>, respectively) occurred during the same time frame (2200–2220 UTC, Fig. 6a). This suggests that an electric dipole formed at low levels due to the differential sedimentation of charged hydrometeors, influenced by the mean storm-relative winds.

The  $Z_{DR}$  and  $K_{DP}$  column volume reached local maximum values 5–10 minutes prior to the first lightning jump at 2110 UTC, but experienced a rapid decrease immediately afterward (Fig. 10a). Overall, despite some fluctuations, the  $K_{DP}$  column volume generally increased after 2120 UTC, reaching its relative maximum value within 5 minutes prior to subsequent lightning jumps, followed by a sudden decline immediately after each jump. The lightning jump at 2220 UTC, however, was an exception, as the  $K_{DP}$  column volume reached a local minimum value around the same time, suggesting a lower overall LWC at this particular time. This characteristic aligns with the observations of Schultz et al. (2015), who noted that not all lightning jumps exhibit the same characteristics. These authors found that a lightning jump can occur even with a decreasing trend in the updraft volume, as secondary ice generation processes (Hallett and Mossop 1974) can lead to ice multiplication through the splintering of graupel and/or fracturing of freezing drops between the -3° and -8°C levels. Thus, despite relatively weak updraft strength (as indicated by the overall decreasing trend in  $Z_{DR}$  column volume), enhanced  $K_{DP}$  values from secondary ice processes (Grazioli et al. 2015; Kumjian et al. 2016; Sinclair et al. 2016) may have been confined to lower levels and significantly contributed to the peak total flash rate in the storm. This mechanism is further supported by the location of maximum flash initiations and source density within the 0° to -10°C levels around 2220 UTC (Fig. 6b and c). In contrast, the temporal evolution of the  $Z_{DR}$  column volume did not exhibit a consistent pattern, making it challenging to establish a clear relationship with the occurrence of lightning jumps.

The correlation between  $K_{DP}$  column volume and total flash rate ( $r = 0.74$ ) was significantly higher compared to the correlation between  $Z_{DR}$  column volume and total flash rate ( $r = -0.34$ ). This finding is consistent with the observations from the Priceville storm and provides additional evidence that variations in  $K_{DP}$  column volume may be more strongly associated with the total

631 flash rate in severe storms within the high-shear environments of southeastern USA, across a range  
632 of low-to-moderate instability conditions. Similar to the Priceville storm, a majority of the flashes  
633 initiated and propagated downshear of the  $Z_{DR}$  and  $K_{DP}$  column objects (Fig. 10b and c). However,  
634 there were some differences in the spatial location. The  $Z_{DR}$  column objects in this storm were  
635 much closer to the lightning activity, flanking the west edge of the maximum source density at all  
636 times (cf. Figs. S13 and S14). Only 37% of the flashes, with a mean area of  $28 \text{ km}^2$ , initiated  
637 within the  $K_{DP}$  column footprint. This percentage was even lower,  $\sim 20\%$  for the  $Z_{DR}$  columns,  
638 which had a mean flash area of  $24 \text{ km}^2$ .

639 (iii) *Case 3 (5 April 2017):* The time-height cross sections for the briefly tornadic supercell  
640 embedded within the QLCS were generated by expanding the search radius to 20 km. This adjust-  
641 ment allowed for the inclusion of transient updrafts in the embedded supercell as the mesoscale  
642 convective system underwent rapid upscale growth. The 30-dBZ echo top height reaching an  
643 altitude of 12 km ARL indicated the presence of intense updrafts (Fig. 8k). Despite the storms  
644 having an earlier onset and longer duration, a 90-minute analysis period (2330 UTC 5 April 2017  
645 to 0015 UTC 6 April 2017) was selected to examine the pretornadic to tornadic transition of the  
646 convective system around 0000 UTC. Positive  $Z_{DR}$  values, ranging from approximately 1 to 4 dB,  
647 were predominantly observed below the ambient  $0^\circ\text{C}$  level at around 4 km (Fig. 8l). However,  
648 using the  $Z_{DR}$  and  $\rho_{hv}$  profiles to discern ongoing microphysical processes posed challenges due  
649 to the complex interactions between updrafts at various stages of their life cycle (Figs. 8l and m).  
650 Low-level  $K_{DP}$  values associated with melting hailstones and heavy rain reached their peak around  
651 2350 UTC (Fig. 8n). The highest VHF source density was centered around 10 km, with reduced  
652 activity at lower levels, particularly between 2330 and 0000 UTC, suggesting a higher fraction  
653 of IC flash activity within the upper-level charge dipole (Fig. 8o). This observation was further  
654 supported by a significant drop in CG flash rate during this time (Fig. 7a).

655 Similar to the previous two cases, the  $K_{DP}$  column volume exhibited a higher correlation with  
656 the total flash rate ( $r = 0.65$ ) compared to  $Z_{DR}$  column volume ( $r = -0.47$ ), as depicted in Fig. 11a.  
657 As mentioned earlier, the subjective nature of isolating flashes associated with the segment of the  
658 QLCS that produced a tornado may have impeded an unbiased quantification of flash initiations in  
659 relation to the spatial orientation of polarimetric signatures. Consequently, a higher proportion of  
660 flash initiations occurred outside the column footprints at  $0^\circ\text{C}$  level (Fig. 11b and c). Specifically,

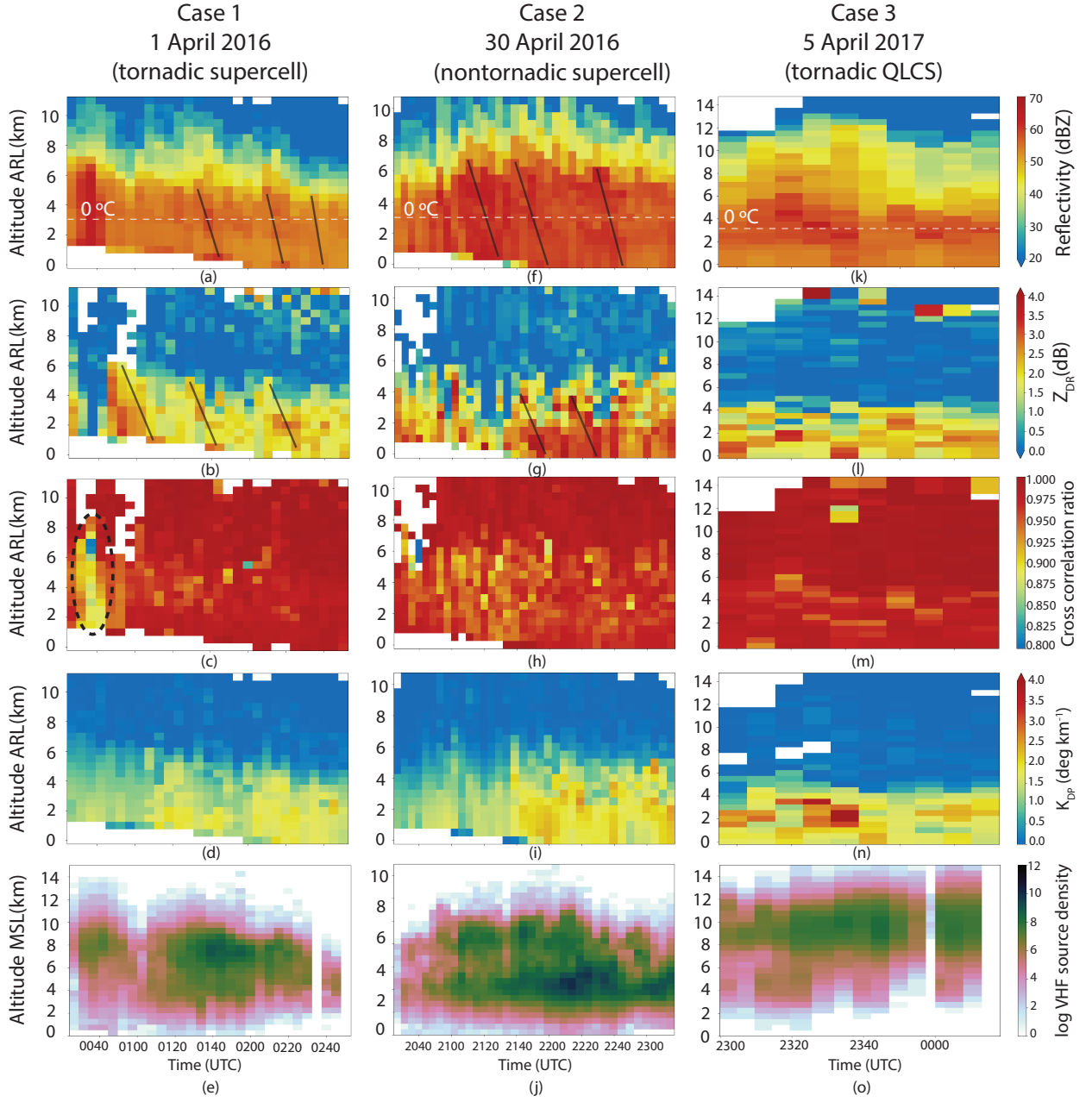
661 23% of lightning flashes, averaging  $16 \text{ km}^2$  in area, initiated within the  $K_{DP}$  column. In contrast,  
662 this percentage decreased to 19.6%, with an average area of  $24 \text{ km}^2$ , for the  $Z_{DR}$  columns.

663 *General comments for all three cases:*

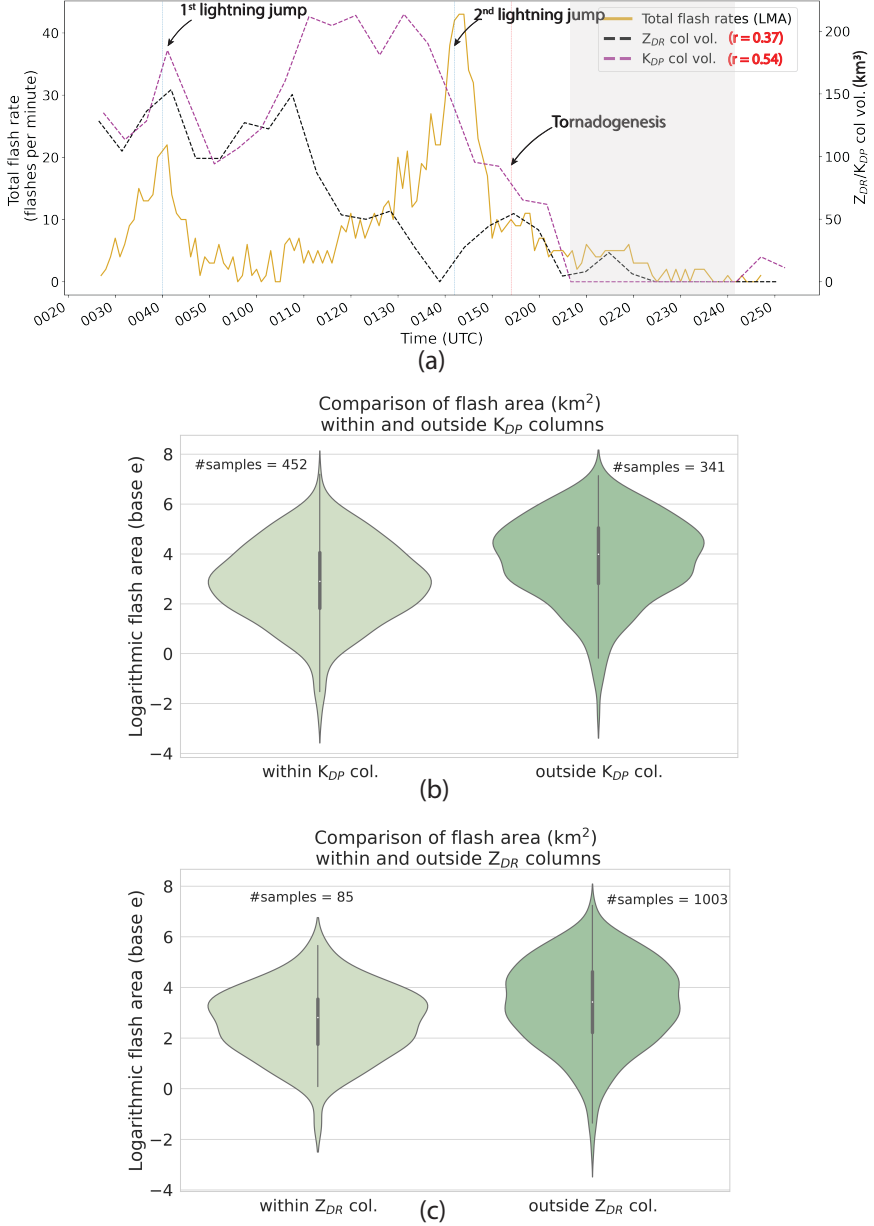
664 The stronger association of total flash rate with the  $K_{DP}$  column volume in all three cases stands  
665 in contrast to the findings from the tornadic supercell near Edmond-Carney, Oklahoma on 19 May  
666 2013 (EC supercell, hereinafter; Sharma et al. 2021), where the  $Z_{DR}$  column volume exhibited a  
667 considerably higher correlation with the flash rate. This contrast suggests that the spatiotemporal  
668 evolution of microphysical processes governing ice formation and charge separation within the  
669 mixed-phase region likely differed significantly between these two storms. This difference could  
670 potentially be attributed to the distinct mesoscale environments of each storm. For instance, except  
671 for the ML CAPE values ( $2783 \text{ J kg}^{-1}$  for EC supercell and  $1118 \text{ J kg}^{-1}$  for Priceville supercell),  
672 other thermodynamic and kinematic variables were greater for the Priceville supercell. This  
673 includes the 0–1 km and 0–3 km SRH ( $159$  and  $273 \text{ m}^2 \text{ s}^{-2}$  for EC supercell, and  $330$  and  $413 \text{ m}^2$   
674  $\text{s}^{-2}$  for Priceville supercell, respectively), as well as the low- and mid-level mean RH values (80%  
675 and 34% for EC supercell, and 88% and 66% for Priceville supercell, respectively). Recent studies  
676 have shown that the growth of ice hydrometeors is significantly modulated by zonal deep layer shear  
677 and vertical distribution of buoyancy, suggesting that the microphysical pathways in high shear  
678 environments can have characteristically different time-scales (Dennis and Kumjian 2017; Nixon  
679 and Allen 2022). The larger warm cloud depth in the EC supercell (3534 m) could be responsible  
680 for the dominance of warm rain processes (Phillips 2024) and a stronger correlation between the  
681  $Z_{DR}$  column volume and total flash rate. In contrast, the warm cloud depth for the storms analyzed  
682 in this study did not exceed 2950 m. Therefore, it is possible that the collision-coalescence process  
683 did not have a head start in the southeastern U.S. storms, and rapid glaciation and subsequent  
684 riming of ice particles contributed to a stronger correlation between the  $K_{DP}$  column volume and  
685 total flash rate.

686 Our analysis indicates that while updrafts were responsible for the noninductive charging of  
687 hydrometeors, the horizontal advection of hydrometeors away from the updraft core (to the east)  
688 due to storm-relative winds caused a spatial rearrangement of charged hydrometeors. A greater  
689 number of small flash initiations outside of the updraft core suggests a dominant role of turbulent  
690 eddies at the eastern periphery of the updrafts, creating local charge pockets with enhanced electric

691 fields. Understanding the details of flash initiation locations is crucial for data assimilation studies,  
692 which use flash extent density to derive pseudo observations of water vapor mixing ratio (Fierro  
693 et al. 2019). When combined with polarimetric signatures (such as the  $Z_{DR}$  column), these data  
694 can be used to update model fields, leading to more accurate storm-scale forecasts (Carlin et al.  
695 2017). While the results of this study suggest that the time-scale of response of microphysical  
696 processes to storm kinematics, as captured by the  $K_{DP}$  column volume, corresponds well the with  
697 the time-scale of fluctuations in total lightning flash rate in southeast U.S. storms, the number of  
698 cases examined is limited. Therefore, caution should be exercised in generalizing these findings.  
699 However, these results raise the possibility that the influence of microphysical processes on storm  
700 dynamics and electrical characteristics can vary depending on their complex interactions with the  
701 buoyancy-shear state space.



702 FIG. 8. Time-height cross sections of KHTX data for all three severe storm cases. (a,f,k) Maximum radar  
 703 reflectivity within the target storm at each vertical grid level. (b,g,l)  $Z_{DR}$  cross sections. Solid black lines in  
 704 panels a and f illustrate the descent of high reflectivity values from upper levels towards the surface. Green lines  
 705 in panels b and g mark the descent of high  $Z_{DR}$  values towards the surface. (c,h,m)  $\rho_{hv}$  cross section (d,i,n)  
 706  $K_{DP}$  cross section. Dashed black polygon in (c) highlights reduced  $\rho_{hv}$  due to three-body scatter spike. (e,j,o)  
 707 Horizontally integrated NALMA VHF source density within the target storm. The white dashed line in (a,f,k)  
 708 denotes the environmental  $0^{\circ}\text{C}$  level above the radar altitude (KHTX altitude = 566 m MSL).



709 FIG. 9. (a) Time series of total lightning flash rate,  $Z_{DR}$  column volume (from KHTX), and  $K_{DP}$  column  
 710 volume (from ARMOR) for the tornadic supercell near Priceville, Alabama on 1 April 2016. Lightning jumps  
 711 and tornadogenesis are marked as light blue and light red vertical lines, respectively. Violin plots of flash area  
 712 within and outside of (b)  $K_{DP}$  column footprint, and (c)  $Z_{DR}$  column footprint at the environmental 0°C level.  
 713 The sample size, representing the number of flashes that meet the criteria in each scenario, is listed on top of each  
 714 plot. A logarithmic scale is used on the y-axes in panels b and c. The shaded region in (a) corresponds to the  
 715 time period when the storm was partially within ARMOR's cone of silence, leading to an incomplete sampling  
 716 of  $K_{DP}$  columns.

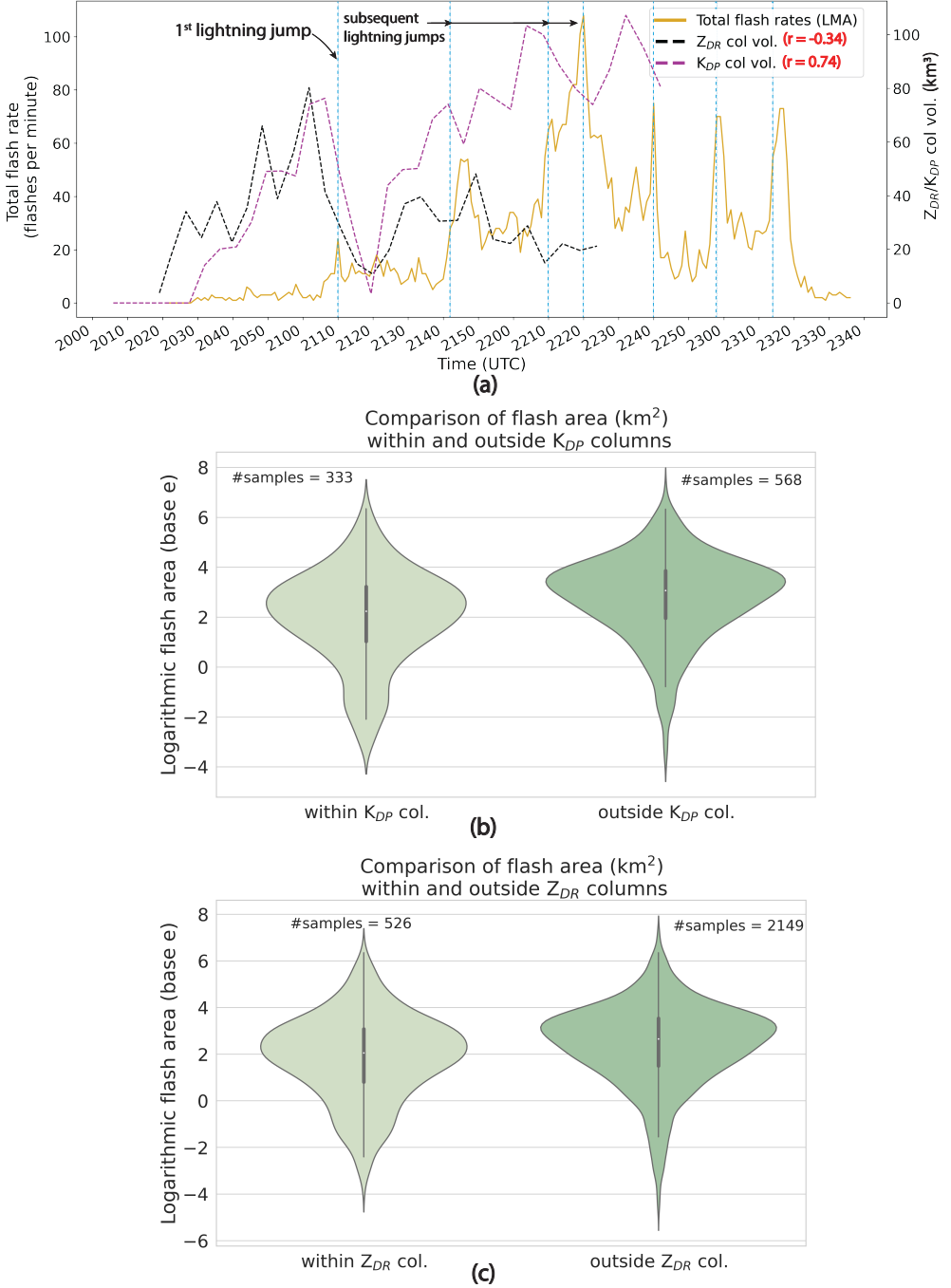


FIG. 10. Same as Fig. 9, except for the nontornadic supercell near Athens, Alabama on 30 April 2016.

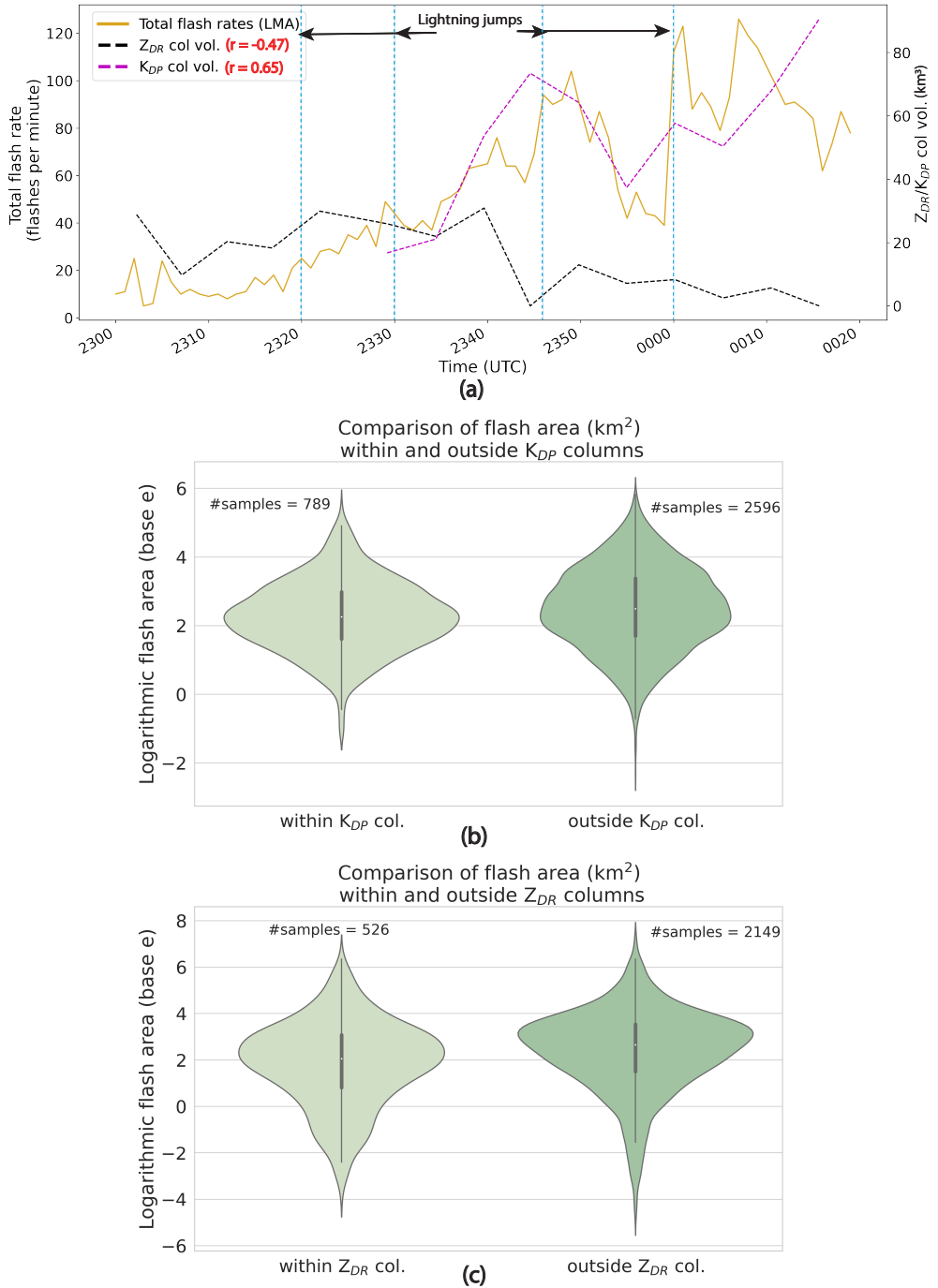


FIG. 11. Same as Fig. 9, except for the supercell embedded within QLCS on 5 April 2017.

717 **5. Summary and Discussion**

718 The goal of this study was to quantify the physical linkage between storm-scale microphysical  
719 processes and cloud electrification via their interrelationship with mixed-phase updrafts. We  
720 analyzed the characteristics of polarimetric signatures and lightning activity in three severe storms  
721 observed during the VORTEX-SE 2016-17 field campaign. These cases included a tornadic  
722 supercell embedded in stratiform precipitation, a nontornadic supercell, and a supercell embedded  
723 within a QLCS. Although we examined only three storms, these cases are representative of the  
724 complex severe convective storms that are typical in the southeastern United States. During all  
725 three cases, synoptic and mesoscale ascent in the narrow unstable warm sector and along the  
726 cold front destabilized the boundary layer and initiated convection. The tornadic and nontornadic  
727 supercells developed in environments characterized by ML CAPE of less than 1150 and 700 J kg<sup>-1</sup>,  
728 respectively, and 0–6 km layer shear exceeding 23 m s<sup>-1</sup>. The rapid upscale growth of the QLCS  
729 was facilitated by strong deep layer BWD of 41 m s<sup>-1</sup>, combined with an ML CAPE exceeding  
730 1300 J kg<sup>-1</sup>. The total lightning flash rate varied significantly among these cases, allowing for a  
731 comparison of the effectiveness of polarimetric indicators in assisting forecasters with assessing  
732 the risk of severe weather during real-time forecasting operations. Here is a brief summary of the  
733 key findings from the observational analysis:

- 734 • In all three cases, K<sub>DP</sub> column volume outperformed Z<sub>DR</sub> column volume as a predictor of  
735 total lightning flash rate (Figs. 9, 10, and 11). The contrast with findings from an isolated  
736 tornadic supercell over the Great Plains, where a stronger correlation was observed between  
737 the Z<sub>DR</sub> column volume and flash rate (Sharma et al. 2021), highlights the significance of the  
738 current study.
- 739 • The early stages of storm life cycle, marked by more steady updrafts, showed a monotonic  
740 increase in the Z<sub>DR</sub> column volume and total flash rate. However, as the updrafts transitioned to  
741 a non-steady state later on, they became less effective at vertical size sorting and recirculation  
742 of supercooled cloud condensate. This led to reduced correlation between the Z<sub>DR</sub> column  
743 volume and total flash rate.
- 744 • The stronger correlation between the K<sub>DP</sub> column volume and total flash rate suggests a  
745 higher contribution of partially melted ice and/or wet/mixed-phase hydrometeors in storm

746 electrification. The relatively shallow warm cloud depth of these storms, compared to the EC  
747 storm in Oklahoma, likely increased the influence of cold cloud processes on ice and graupel  
748 growth, thereby modulating total flash rates.

- 749 • The peak CG and total flash rates in the tornadic and nontornadic supercells were observed to  
750 coincide with the descent of precipitation shafts that transported melting graupel or hail to the  
751 surface. Furthermore, there was a notable increase in the bi-level VHF source density during  
752 these periods, indicating a direct role of charge advection in the creation of electric potential  
753 wells that facilitate the propagation of lightning discharges (Figs. 8a-f).

744 Our central hypothesis was based on the assumption that updraft vertical velocity (or updraft  
745 mass flux) exhibits a linear relationship with the volume of  $Z_{DR}$  and  $K_{DP}$  columns, and this  
746 relationship extends to total lightning flash rates. While  $Z_{DR}$  and  $K_{DP}$  column properties provide  
747 valuable insights, they may not directly correspond to specific updraft speed values. Rather,  
748 they can be used to assess important qualitative changes related to updraft intensity. As shown  
749 in this study, the volume of these columnar features does not consistently follow a monotonic  
750 relationship with total lightning flash rate, suggesting the possibility of other factors influencing  
751 this relationship. Grant et al. (2022) found that the updraft vertical velocity in a simulated supercell  
752 demonstrated the strongest linear relationship with total water condensate (liquid and ice) only  
753 within the temperature range of -10° to -30°C. This correlation tended to decrease within -15° to  
754 -5°C layer, which constitutes bulk of the  $Z_{DR}$  and  $K_{DP}$  column volume at lower altitudes. The  
755 authors attributed this reduction in correlation to liquid-ice phase changes and a deep-layer inflow  
756 leading to enhanced supersaturation in the southeast portion of the main updraft. Additionally,  
757 several observational studies utilizing multi-Doppler wind synthesis have reported instances where  
758 the  $Z_{DR}$  columns were spatially offset to the east of the primary updraft (Wienhoff et al. 2018;  
759 Montopoli et al. 2021). It is difficult to assume a strong linear correlation between the  $Z_{DR}$  column  
760 volume and updraft speed when the two are not collocated at mid-levels, potentially challenging  
761 our initial assumption.

762 Furthermore, the life cycle of  $Z_{DR}$  and  $K_{DP}$  columns may not be synchronized in time with  
763 each other or with the updraft intensity. As noted in Kumjian et al. (2010), the mid-level areal  
764 extent of  $K_{DP}$  and  $Z_{DR}$  columns in supercells can have competing effects. These authors found that  
765 when the  $K_{DP}$  column expanded, the  $Z_{DR}$  column shrank, resulting in the highest overlap during

776 precipitation fallout. Greater overlap between the two columns suggested the presence of weaker  
777 updraft and larger hail, resulting in a reduced  $Z_{DR}$  column footprint, while  $K_{DP}$  columns remained  
778 unaffected. In contrast, stronger updrafts are typically associated with high  $Z_{DR}$  and low  $K_{DP}$   
779 values (Kumjian et al. 2010). The larger  $K_{DP}$  column volumes and lower  $Z_{DR}$  values in this study  
780 suggest weaker mid-level updrafts in the moisture-rich, high-shear environments of the southeast  
781 U.S., which were less efficient at recirculating raindrops into the updraft core compared to those in  
782 the central Great Plains. van Lier-Walqui et al. (2016) also found a strong, but lagged correlation  
783 between  $K_{DP}$  column volume and updraft mass flux. They also reported that temporal trends in  
784  $Z_{DR}$  columns may better capture the early stages of deep convective evolution while  $K_{DP}$  columns  
785 may be better suited for later stages when ice processes (generating these columns) are more active.  
786 We noticed the delayed appearance of  $K_{DP}$  columns in cases 2 and 3 in this study. Furthermore, the  
787  $Z_{DR}$  column volume increased monotonically with the total lightning flash rate in the early stages  
788 of the storm in cases 1 and 3. Therefore, it may be useful to account for the temporal evolution of  
789 both columnar features while inferring updraft strength throughout the storm life cycle.

790 Finally, differential attenuation and nonuniform beam filling in the mixed-phase region, as well  
791 as poor vertical resolution at greater ranges from WSR-88D can impede the accurate estimation  
792 of  $Z_{DR}$  column volume. Otherwise, the presence of large hail within or near the updraft core  
793 can introduce excessive noise or cause extremely low  $Z_{DR}$  values, resulting in the demise of  $Z_{DR}$   
794 columns. We noticed this phenomenon in several KHTX volume scans, where a  $Z_{DR}$  column  
795 object was momentarily disrupted only to reappear in subsequent scans. Similarly,  $K_{DP}$  estimation  
796 can suffer from significant backscatter differential phase and cross-coupling effects in the mixed  
797 and ice-phase regions (Giangrande et al. 2013; Hubbert et al. 2014; Reimel and Kumjian 2021).

798 Nonetheless, the results of this study have significant implications for the development of algo-  
799 rithms that leverage polarimetric and lightning data. These algorithms could enhance real-time  
800 severe weather warning operations by tracking updraft evolution or by assimilating radar and  
801 lightning observations to improve the accuracy of severe weather forecasts. For example, rapid  
802 increases (or a jump) in the frequency of small-sized lightning flashes (area  $< 4 \text{ km}^2$ ), occurring in  
803 close spatial and temporal proximity to an expanding  $Z_{DR}$  column footprint, can alert forecasters  
804 to intensifying updrafts. This information can prompt them to monitor the corresponding storm  
805 region closely for potential near-term hazards (Schultz et al. 2015; Krause and Klaus 2024). Light-

ning jumps associated with an expanding  $K_{DP}$  column volume may not directly indicate updraft intensification. Instead, they could signal an increased potential for hail fallout, intense downdraft cores, and surface wind damage (Kuster et al. 2021). A greater overlap between the cluster of flash initiations and the  $Z_{DR}$  column core may help identify whether flashes are initiating in regions with highly turbulent updraft edges characterized by larger horizontal gradients in updraft velocity (Stough et al. 2022). When flash initiations occur outside the  $Z_{DR}$  and  $K_{DP}$  columns, they can help identify exact locations for adjusting moisture and latent heat within the updraft region (from  $Z_{DR}$  and  $K_{DP}$  columns) and outside the updraft (flash initiation cluster) in numerical model forecasts. This better captured spatial heterogeneity in thermodynamic perturbations can lead to more accurate storm-scale analyses (Carlin et al. 2017; Fierro et al. 2019).

We have demonstrated that lightning flash rate and size data provide an additional microphysical and dynamical signal that is meaningfully different from  $Z_{DR}$  and  $K_{DP}$  column volume. Even when weak mid-level updrafts may struggle with vertical size sorting of hydrometeors or the storm's range from the radar hinders continuous monitoring of  $Z_{DR}$  and  $K_{DP}$  column volume, an increase in total lightning flash rates and a higher percentage of small, short-lived flashes can provide valuable insights into updraft intensification (Calhoun et al. 2013; Bruning and MacGorman 2013). Additionally, accounting for metrics associated with the evolution of  $Z_{DR}$  and  $K_{DP}$  columns may enhance the performance of single-parameter flash rate parameterization schemes used to simulate lightning flashes in numerical models. Periods of updraft intensification may more accurately reflect the contemporaneous increase in both  $Z_{DR}$  column and the flash initiation rate, while periods of precipitation fallout and/or active riming of ice crystals by cloud droplet accretion may better correspond to the expansion of  $K_{DP}$  columns and the simultaneous increase in flash initiation rate. The relative weighting assigned to each column signature may need to be evaluated for other convective modes and for storms in varied background conditions, such as cold versus very warm cloud base, and vertical distribution of buoyancy and free tropospheric environmental humidity, among others. Future studies should examine  $Z_{DR}$  and  $K_{DP}$  column variations in diverse mesoscale environments, covering a broad spectrum of buoyancy-shear state space. Long-term observations of polarimetric signatures using collocated radar wind profilers and vertically pointing radars for various convective modes and geographical locations can help better understand the relationship between updraft mass flux and the extent of  $Z_{DR}$  and  $K_{DP}$  columns. When combined with numerical

836 simulations, these observations can shed light on the microphysical pathways that link polarimetric  
837 signatures with updraft dynamics and storm electrification.

838 *CRediT (Contributor Roles Taxonomy) statement.* MS: Conceptualization, data curation, formal  
839 analysis, investigation, methodology, software, visualization, writing – original draft. RLT: Su-  
840 pervision, funding acquisition, project administration, resources, validation, writing – review and  
841 editing. ECB: Supervision, software, funding acquisition, writing – review and editing.

842 *Acknowledgments.* The lead author extends heartfelt appreciation to Drs. Daniel T. Dawson II  
843 and Wen-wen Tung for their invaluable mentorship during his graduate studies. Thanks go to all  
844 involved in collecting radiosonde and radar observations during VSE 2016-17. We are grateful to  
845 Vaisala Inc. for providing NLDN data. Discussions with the three anonymous reviewers, Jami  
846 Boettcher (NSSL/CIWRO), and Jordan Brook (Australian Bureau of Meteorology) significantly  
847 improved this paper. We would also like to thank the creators of and contributors to several open  
848 source Python software packages, especially PyART (Helmus and Collis 2016), NumPy (Harris  
849 et al. 2020), SciPy (Virtanen et al. 2020), xarray (Hoyer and Hamman 2017), MetPy (May et al.  
850 2008), and SHARPpy v1.4.0 (Blumberg et al. 2017) which were used in this study. Most of the  
851 data visualization for this study was performed using matplotlib (Hunter 2007). This research  
852 was funded by the U.S. Department of Commerce, under the NOAA award NA19OAR4590209.  
853 The statements, findings, conclusions, and recommendations are those of the authors' and do not  
854 necessarily reflect the views of the NOAA or the U.S. Department of Commerce.

855 *Data availability statement.* KHTX level-II data were obtained from the National Centers for  
856 Environmental Information (NCEI) NEXRAD data inventory (NOAA National Weather Service  
857 (NWS) Radar Operations Center 1991), while ARMOR data files were downloaded from the  
858 National Center for Atmospheric Research (NCAR) Earth Observing Laboratory (EOL) archive  
859 (Carey and Vacek 2017). NALMA data corresponding to these were obtained from the NCAR  
860 EOL archive (Carey and Stough 2017) and NASA Global Hydrology Resource Center (GHRC;  
861 Blakeslee 2019), respectively. NLDN data are an access controlled commercial dataset held by  
862 Vaisala.

863    **References**

- 864    Barnes, S. L., 1964: A Technique for Maximizing Details in Numerical Weather Map Analysis.  
865    *J. Appl. Meteor. Climatol.*, **3** (4), 396–409, [https://doi.org/10.1175/1520-0450\(1964\)003<0396:ATFMDI>2.0.CO;2](https://doi.org/10.1175/1520-0450(1964)003<0396:ATFMDI>2.0.CO;2).
- 866  
867    Basarab, B. M., S. A. Rutledge, and B. R. Fuchs, 2015: An improved lightning flash rate pa-  
868    rameterization developed from Colorado DC3 thunderstorm data for use in cloud-resolving  
869    chemical transport models. *J. Geophys. Res. Atmos.*, **120** (18), 9481–9499, <https://doi.org/10.1002/2015JD023470>.
- 870  
871    Bedka, K. M., C. Wang, R. Rogers, L. D. Carey, W. Feltz, and J. Kanak, 2015: Examining deep  
872    convective cloud evolution using total lightning, wsr-88d, and goes-14 super rapid scan datasets.  
873    *Wea. Forecasting*, **30** (3), 571 – 590, <https://doi.org/10.1175/WAF-D-14-00062.1>,  
874    URL [https://journals.ametsoc.org/view/journals/wefo/30/3/waf-d-14-00062\\_1.xml](https://journals.ametsoc.org/view/journals/wefo/30/3/waf-d-14-00062_1.xml).
- 875  
876    Blakeslee, R., 2019: GOES-R PLT north alabama lightning mapping array (LMA). NASA  
877    Global Hydrometeorology Resource Center DAAC, <https://doi.org/10.5067/GOESRPLT/LMA/DATA401>.
- 878  
879    Bluestein, H. B., and D. R. MacGorman, 1998: Evolution of Cloud-to-Ground Lightning  
880    Characteristics and Storm Structure in the Spearman, Texas, Tornadic Supercells of 31 May  
881    1990. *Mon. Wea. Rev.*, **126** (6), 1451–1467, [https://doi.org/10.1175/1520-0493\(1998\)126<1451:EOCTGL>2.0.CO;2](https://doi.org/10.1175/1520-0493(1998)126<1451:EOCTGL>2.0.CO;2).
- 882  
883    Blumberg, W. G., K. T. Halbert, T. A. Supinie, P. T. Marsh, R. L. Thompson, and J. A.  
884    Hart, 2017: Sharppy: An open-source sounding analysis toolkit for the atmospheric sci-  
885    ences. *Bulletin of the American Meteorological Society*, **98** (8), 1625–1636, <https://doi.org/10.1175/BAMS-D-15-00309.1>, URL <https://github.com/sharppy/SHARPpy>.
- 886  
887    Boccippio, D. J., K. L. Cummins, H. J. Christian, and S. J. Goodman, 2001: Com-  
888    bined satellite- and surface-based estimation of the intracloud–cloud-to-ground lightning ra-  
889    tio over the continental united states. *Mon. Wea. Rev.*, **129** (1), 108 – 122, [https://doi.org/10.1175/1520-0493\(2001\)129<0108:CSASBE>2.0.CO;2](https://doi.org/10.1175/1520-0493(2001)129<0108:CSASBE>2.0.CO;2), URL [https://journals.ametsoc.org/view/journals/mwre/129/1/1520-0493\\_2001\\_129\\_0108\\_casbe\\_2.0.co\\_2.xml](https://journals.ametsoc.org/view/journals/mwre/129/1/1520-0493_2001_129_0108_casbe_2.0.co_2.xml).
- 890

- 891 Brandes, E. A., J. Vivekanandan, J. D. Tuttle, and C. J. Kessinger, 1995: A Study of Thunderstorm  
892 Microphysics with Multiparameter Radar and Aircraft Observations. *Mon. Wea. Rev.*, **123** (11),  
893 3129–3143, [https://doi.org/10.1175/1520-0493\(1995\)123<3129:ASOTMW>2.0.CO;2](https://doi.org/10.1175/1520-0493(1995)123<3129:ASOTMW>2.0.CO;2).
- 894 Bringi, V. N., D. A. Burrows, and S. M. Menon, 1991: Multiparameter Radar and Aircraft Study of  
895 Raindrop Spectral Evolution in Warm-based Clouds. *J. Appl. Meteor. Climatol.*, **30** (6), 853–880,  
896 [https://doi.org/10.1175/1520-0450\(1991\)030<0853:MRAASO>2.0.CO;2](https://doi.org/10.1175/1520-0450(1991)030<0853:MRAASO>2.0.CO;2).
- 897 Bringi, V. N., K. Knupp, A. Detwiler, L. Liu, I. J. Caylor, and R. A. Black, 1997: Evolution  
898 of a Florida Thunderstorm during the Convection and Precipitation/Electrification Experiment:  
899 The Case of 9 August 1991. *Mon. Wea. Rev.*, **125** (9), 2131–2160, [https://doi.org/10.1175/1520-0493\(1997\)125<2131:EOAFTD>2.0.CO;2](https://doi.org/10.1175/1520-0493(1997)125<2131:EOAFTD>2.0.CO;2).
- 900 Bringi, V. N., L. Liu, P. C. Kennedy, V. Chandrasekar, and S. A. Rutledge, 1996: Dual multipa-  
901 rameter radar observations of intense convective storms: The 24 June 1992 case study. *Meteorol.*  
902 *Atmos. Phys.*, **59** (1), 3–31, <https://doi.org/10.1007/BF01031999>.
- 903 Bruning, E. C., 2015: Lmatoools: Lmatoools-v0.5z-stable. Zenodo, <https://doi.org/10.5281/zenodo.32510>.
- 904 Bruning, E. C., and D. R. MacGorman, 2013: Theory and Observations of Controls on Lightning  
905 Flash Size Spectra. *J. Atmos. Sci.*, **70** (12), 4012–4029, <https://doi.org/10.1175/JAS-D-12-0289.1>.
- 906 Bruning, E. C., S. A. Weiss, and K. M. Calhoun, 2014: Continuous variability in thunderstorm  
907 primary electrification and an evaluation of inverted-polarity terminology. *Atmos. Res.*, **135–136**,  
908 274–284, <https://doi.org/10.1016/j.atmosres.2012.10.009>.
- 909 Calhoun, K. M., D. R. MacGorman, C. L. Ziegler, and M. I. Biggerstaff, 2013: Evolution of Light-  
910 ning Activity and Storm Charge Relative to Dual-Doppler Analysis of a High-Precipitation Super-  
911 cell Storm. *Mon. Wea. Rev.*, **141** (7), 2199–2223, <https://doi.org/10.1175/MWR-D-12-00258.1>.
- 912 Calhoun, K. M., E. R. Mansell, D. R. MacGorman, and D. C. Dowell, 2014: Numerical Simulations  
913 of Lightning and Storm Charge of the 29–30 May 2004 Geary, Oklahoma, Supercell Thunder-  
914 storm Using EnKF Mobile Radar Data Assimilation. *Mon. Wea. Rev.*, **142** (11), 3977–3997,  
915 <https://doi.org/10.1175/MWR-D-13-00403.1>.

- 919 Carey, L., and S. Stough, 2017: North alabama lightning mapping array (NALMA) data. Version  
920 1.1. UCAR/NCAR - Earth Observing Laboratory, <https://doi.org/10.5065/D6Z899T8>.
- 921 Carey, L., and A. Vacek, 2017: UAH ARMOR C-band radar data. Version 1.0. UCAR/NCAR -  
922 Earth Observing Laboratory, <https://doi.org/10.5065/D6WQ0276>.
- 923 Carey, L. D., and S. A. Rutledge, 1996: A multiparameter radar case study of the microphysical  
924 and kinematic evolution of a lightning producing storm. *Meteorol. Atmos. Phys.*, **59** (1), 33–64,  
925 <https://doi.org/10.1007/BF01032000>.
- 926 Carey, L. D., and S. A. Rutledge, 1998: Electrical and multiparameter radar observations of a  
927 severe hailstorm. *J. Geophys. Res. Atmos.*, **103** (D12), 13 979–14 000, <https://doi.org/10.1029/97JD02626>.
- 928 Carey, L. D., and S. A. Rutledge, 2000: The Relationship between Precipitation and Lightning  
929 in Tropical Island Convection: A C-Band Polarimetric Radar Study. *Mon. Wea. Rev.*, **128** (8),  
930 2687–2710, [https://doi.org/10.1175/1520-0493\(2000\)128<2687:TRBPAL>2.0.CO;2](https://doi.org/10.1175/1520-0493(2000)128<2687:TRBPAL>2.0.CO;2).
- 931 Carey, L. D., E. V. Schultz, C. J. Schultz, W. Deierling, W. A. Petersen, A. L. Bain, and K. E.  
932 Pickering, 2019: An Evaluation of Relationships between Radar-Inferred Kinematic and Micro-  
933 physical Parameters and Lightning Flash Rates in Alabama Storms. *Atmosphere*, **10** (12), 796,  
934 <https://doi.org/10.3390/atmos10120796>.
- 935 Carlin, J. T., J. Gao, J. C. Snyder, and A. V. Ryzhkov, 2017: Assimilation of zdr columns  
936 for improving the spinup and forecast of convective storms in storm-scale models: Proof-  
937 of-concept experiments. *Monthly Weather Review*, **145** (12), 5033 – 5057, <https://doi.org/10.1175/MWR-D-17-0103.1>, URL <https://journals.ametsoc.org/view/journals/mwre/145/12/mwr-d-17-0103.1.xml>.
- 938 Caylor, I. J., and A. J. Illingworth, 1987: Radar Observations and Modelling of Warm Rain Initia-  
939 tion. *Q. J. R. Meteorolog. Soc.*, **113** (478), 1171–1191, <https://doi.org/10.1002/qj.49711347806>.
- 940 Chasteen, M. B., and S. E. Koch, 2022a: Multiscale Aspects of the 26–27 April 2011 Tornado  
941 Outbreak. Part I: Outbreak Chronology and Environmental Evolution. *Mon. Wea. Rev.*, **150** (2),  
942 309–335, <https://doi.org/10.1175/MWR-D-21-0013.1>.

- 946 Chasteen, M. B., and S. E. Koch, 2022b: Multiscale Aspects of the 26–27 April 2011 Tornado  
947 Outbreak. Part II: Environmental Modifications and Upscale Feedbacks Arising from Latent  
948 Processes. *Mon. Wea. Rev.*, **150** (2), 337–368, <https://doi.org/10.1175/MWR-D-21-0014.1>.
- 949 Chernyaev, E. V., 1995: Marching cubes 33: Construction of topologically correct isosurfaces.  
950 Tech. rep.
- 951 Chmielewski, V. C., J. Blair, D. Kennedy, D. MacGorman, and K. M. Calhoun, 2022: A Compari-  
952 son of Processing Methods for the Oklahoma Lightning Mapping Array. *Earth Space Sci.*, **9** (7),  
953 e2021EA002081, <https://doi.org/10.1029/2021EA002081>.
- 954 Chmielewski, V. C., and E. C. Bruning, 2016: Lightning Mapping Array flash detection per-  
955 formance with variable receiver thresholds. *J. Geophys. Res. Atmos.*, **121** (14), 8600–8614,  
956 <https://doi.org/10.1002/2016JD025159>.
- 957 Conway, J. W., and D. S. Zrnić, 1993: A Study of Embryo Production and Hail Growth Using  
958 Dual-Doppler and Multiparameter Radars. *Mon. Wea. Rev.*, **121** (9), 2511–2528, [https://doi.org/10.1175/1520-0493\(1993\)121<2511:ASOEPA>2.0.CO;2](https://doi.org/10.1175/1520-0493(1993)121<2511:ASOEPA>2.0.CO;2).
- 960 Crowe, C. C., C. J. Schultz, M. Kumjian, L. D. Carey, and W. A. Petersen, 2012: Use of dual-  
961 polarization signatures in diagnosing tornadic potential. *Electron. J. Oper. Meteor.*, **13** (5),  
962 57–78.
- 963 Curran, E. B., and W. D. Rust, 1992: Positive Ground Flashes Produced by Low-Precipitation  
964 Thunderstorms in Oklahoma on 26 April 1984. *Mon. Wea. Rev.*, **120** (4), 544–553, [https://doi.org/10.1175/1520-0493\(1992\)120<0544:PGFPBL>2.0.CO;2](https://doi.org/10.1175/1520-0493(1992)120<0544:PGFPBL>2.0.CO;2).
- 966 Davis, J. M., and M. D. Parker, 2014: Radar Climatology of Tornadic and Nontornadic Vortices  
967 in High-Shear, Low-CAPE Environments in the Mid-Atlantic and Southeastern United States.  
968 *Wea. Forecasting*, **29** (4), 828–853, <https://doi.org/10.1175/WAF-D-13-00127.1>.
- 969 Dean, A. R., 2008: Forecast challenges at the NWS Storm Prediction Center relating to the  
970 frequency of favorable severe storm environments. *24th Conference on Severe Local Storms*  
971 (27–31 October 2008), AMS, URL <https://ams.confex.com/ams/pdffiles/141743.html>.

- 972 Dean, A. R., and R. S. Schneider, 2012: An examination of tornado environments, events, and  
973 impacts from 2003–2012. *26th Conf. on Severe Local Storms*, URL <https://ams.confex.com/ams/26SLS/webprogram/Paper211580.html>.
- 975 Deierling, W., and W. A. Petersen, 2008: Total lightning activity as an indicator of updraft  
976 characteristics. *J. Geophys. Res. Atmos.*, **113 (D16)**, <https://doi.org/10.1029/2007JD009598>.
- 977 Deierling, W., W. A. Petersen, J. Latham, S. Ellis, and H. J. Christian, 2008: The relationship  
978 between lightning activity and ice fluxes in thunderstorms. *J. Geophys. Res. Atmos.*, **113 (D15)**,  
979 <https://doi.org/10.1029/2007JD009700>.
- 980 Dennis, E. J., and M. R. Kumjian, 2017: The Impact of Vertical Wind Shear on Hail Growth in  
981 Simulated Supercells. *J. Atmos. Sci.*, **74 (3)**, 641–663, <https://doi.org/10.1175/JAS-D-16-0066.1>.
- 982 Doswell, C. A., and D. Burgess, 1993: Tornadoes and tornadic storms: A review of concep-  
983 tual models. *The Tornado: Its Structure, Dynamics, Prediction, and Hazards*, C. R. Church,  
984 D. Burgess, C. A. Doswell, and R. Davies-Jones, Eds., Vol. 79, American Geophysical Union,  
985 161–172.
- 986 Emersic, C., P. L. Heinselman, D. R. MacGorman, and E. C. Bruning, 2011: Lightning ac-  
987 tivity in a hail-producing storm observed with phased-array radar. *Monthly Weather Review*,  
988 **139 (6)**, 1809 – 1825, <https://doi.org/10.1175/2010MWR3574.1>, URL <https://journals.ametsoc.org/view/journals/mwre/139/6/2010mwr3574.1.xml>.
- 989 Ester, M., H.-P. Kriegel, J. Sander, and X. Xu, 1996: A density-based algorithm for discovering  
990 clusters in large spatial databases with noise. *Proceedings of the Second International Conference  
991 on Knowledge Discovery and Data Mining*, AAAI Press, Portland, Oregon, 226–231, KDD’96.
- 992 Fierro, A. O., Y. Wang, J. Gao, and E. R. Mansell, 2019: Variational assimilation of radar data and  
993 glm lightning-derived water vapor for the short-term forecasts of high-impact convective events.  
994 *Monthly Weather Review*, **147 (11)**, 4045 – 4069, <https://doi.org/10.1175/MWR-D-18-0421.1>,  
995 URL <https://journals.ametsoc.org/view/journals/mwre/147/11/mwr-d-18-0421.1.xml>.
- 996 French, M. M., and D. M. Kingfield, 2021: Tornado Formation and Intensity Prediction Using Po-  
997 larimetric Radar Estimates of Updraft Area. *Wea. Forecasting*, **36 (6)**, 2211–2231, <https://doi.org/10.1175/WAF-D-21-0087.1>.

- 1000 Fridlind, A. M., and Coauthors, 2019: Use of polarimetric radar measurements to constrain  
1001 simulated convective cell evolution: A pilot study with Lagrangian tracking. *Atmospheric*  
1002 *Measurement Techniques*, **12** (6), 2979–3000, <https://doi.org/10.5194/amt-12-2979-2019>, URL  
1003 <https://amt.copernicus.org/articles/12/2979/2019/>.
- 1004 Fuchs, B. R., E. C. Bruning, S. A. Rutledge, L. D. Carey, P. R. Krehbiel, and W. Rison, 2016:  
1005 Climatological analyses of LMA data with an open-source lightning flash-clustering algorithm.  
1006 *J. Geophys. Res. Atmos.*, **121** (14), 8625–8648, <https://doi.org/10.1002/2015JD024663>.
- 1007 Giangrande, S. E., R. McGraw, and L. Lei, 2013: An Application of Linear Programming to  
1008 Polarimetric Radar Differential Phase Processing. *J. Atmos. Oceanic Technol.*, **30** (8), 1716–  
1009 1729, <https://doi.org/10.1175/JTECH-D-12-00147.1>.
- 1010 Goodman, S., and Coauthors, 2005: The north alabama lightning mapping array: Recent severe  
1011 storm observations and future prospects. *Atmos. Res.*, **76** (1), 423–437, <https://doi.org/https://doi.org/10.1016/j.atmosres.2004.11.035>, URL <https://www.sciencedirect.com/science/article/pii/S0169809505000645>, atmospheric Electricity.
- 1014 Goodnight, J. S., D. A. Chehak, and R. J. Trapp, 2022: Quantification of QLCS Tornadogenesis,  
1015 Associated Characteristics, and Environments across a Large Sample. *Wea. Forecasting*, **37** (11),  
1016 2087–2105, <https://doi.org/10.1175/WAF-D-22-0016.1>.
- 1017 Grant, L. D., S. C. van den Heever, Z. S. Haddad, J. Bukowski, P. J. Marinescu, R. L. Storer, D. J.  
1018 Posselt, and G. L. Stephens, 2022: A linear relationship between vertical velocity and condensa-  
1019 tion processes in deep convection. *J. Atmos. Sci.*, **79** (2), 449 – 466, <https://doi.org/https://doi.org/10.1175/JAS-D-21-0035.1>, URL <https://journals.ametsoc.org/view/journals/atsc/79/2/JAS-D-21-0035.1.xml>.
- 1022 Gravelle, C. M., J. R. Mecikalski, W. E. Line, K. M. Bedka, R. A. Petersen, J. M. Sieglaff,  
1023 G. T. Stano, and S. J. Goodman, 2016: Demonstration of a goes-r satellite convective  
1024 toolkit to “bridge the gap” between severe weather watches and warnings: An example from  
1025 the 20 may 2013 moore, oklahoma, tornado outbreak. *Bull. Amer. Meteor. Soc.*, **97** (1),  
1026 69 – 84, <https://doi.org/https://doi.org/10.1175/BAMS-D-14-00054.1>, URL <https://journals.ametsoc.org/view/journals/bams/97/1/bams-d-14-00054.1.xml>.

- 1028 Grazioli, J., G. Lloyd, L. Panziera, C. R. Hoyle, P. J. Connolly, J. Henneberger, and A. Berne,  
1029 2015: Polarimetric radar and in situ observations of riming and snowfall microphysics during  
1030 clace 2014. *Atmospheric Chemistry and Physics*, **15** (23), 13 787–13 802, <https://doi.org/10.5194/acp-15-13787-2015>, URL <https://acp.copernicus.org/articles/15/13787/2015/>.  
1031
- 1032 Gupta, A. K., and Coauthors, 2023: The microphysics of the warm-rain and ice crystal processes of  
1033 precipitation in simulated continental convective storms. *Communications Earth & Environment*,  
1034 **4** (1), 226.
- 1035 Hall, M. P. M., J. W. F. Goddard, and S. M. Cherry, 1984: Identification of hydrometeors  
1036 and other targets by dual-polarization radar. *Radio Science*, **19** (1), 132–140, <https://doi.org/10.1029/RS019i001p00132>.
- 1038 Hallett, J., and S. C. Mossop, 1974: Production of secondary ice particles during the riming process.  
1039 *Nature*, **249** (5452), 26–28, <https://doi.org/10.1038/249026a0>, URL <https://www.nature.com/articles/249026a0>.
- 1041 Harris, C. R., and Coauthors, 2020: Array programming with NumPy. *Nature*, **585** (7825), 357–  
1042 362, <https://doi.org/10.1038/s41586-020-2649-2>.
- 1043 Heikenfeld, M., P. J. Marinescu, M. Christensen, D. Watson-Parris, F. Senf, S. C. van den Heever,  
1044 and P. Stier, 2019: Tobac 1.2: Towards a flexible framework for tracking and analysis of  
1045 clouds in diverse datasets. *Geosci. Model Dev.*, **12** (11), 4551–4570, <https://doi.org/10.5194/gmd-12-4551-2019>.
- 1047 Helmus, J., and S. Collis, 2016: The Python ARM Radar Toolkit (Py-ART), a Library for Working  
1048 with Weather Radar Data in the Python Programming Language. *J. Open Res. Softw.*, **4** (1), e25,  
1049 <https://doi.org/10.5334/jors.119>.
- 1050 Homeyer, C. R., and M. R. Kumjian, 2015: Microphysical Characteristics of Overshooting Con-  
1051 vection from Polarimetric Radar Observations. *J. Atmos. Sci.*, **72** (2), 870–891, <https://doi.org/10.1175/JAS-D-13-0388.1>.
- 1053 Hoyer, S., and J. Hamman, 2017: Xarray: N-D labeled arrays and datasets in Python. *J. Open Res.*  
1054 *Softw.*, **5** (1), <https://doi.org/10.5334/jors.148>.

- 1055 Hubbert, J., and V. N. Bringi, 1995: An iterative filtering technique for the analysis of copolar  
1056 differential phase and dual-frequency radar measurements. *J. Atmos. Oceanic Technol.*, **12** (3),  
1057 643 – 648, [https://doi.org/10.1175/1520-0426\(1995\)012<0643:AIFTFT>2.0.CO;2](https://doi.org/10.1175/1520-0426(1995)012<0643:AIFTFT>2.0.CO;2), URL [https://journals.ametsoc.org/view/journals/atot/12/3/1520-0426\\_1995\\_012\\_0643\\_aiftft\\_2\\_0\\_co\\_2.xml](https://journals.ametsoc.org/view/journals/atot/12/3/1520-0426_1995_012_0643_aiftft_2_0_co_2.xml).
- 1060 Hubbert, J., V. N. Bringi, L. D. Carey, and S. Bolen, 1998: CSU-CHILL Polarimetric Radar  
1061 Measurements from a Severe Hail Storm in Eastern Colorado. *J. Appl. Meteor. Climatol.*, **37** (8),  
1062 749–775, [https://doi.org/10.1175/1520-0450\(1998\)037<0749:CCPRMF>2.0.CO;2](https://doi.org/10.1175/1520-0450(1998)037<0749:CCPRMF>2.0.CO;2).
- 1063 Hubbert, J. C., S. M. Ellis, W.-Y. Chang, S. Rutledge, and M. Dixon, 2014: Modeling and Interpre-  
1064 tation of S-Band Ice Crystal Depolarization Signatures from Data Obtained by Simultaneously  
1065 Transmitting Horizontally and Vertically Polarized Fields. *J. Appl. Meteor. Climatol.*, **53** (6),  
1066 1659–1677, <https://doi.org/10.1175/JAMC-D-13-0158.1>.
- 1067 Hueholt, D. M., S. E. Yuter, and M. A. Miller, 2022: Revisiting diagrams of ice growth en-  
1068 vironments. *Bulletin of the American Meteorological Society*, **103** (11), E2584 – E2603,  
1069 <https://doi.org/10.1175/BAMS-D-21-0271.1>, URL <https://journals.ametsoc.org/view/journals/bams/103/11/BAMS-D-21-0271.1.xml>.
- 1071 Hunter, J. D., 2007: Matplotlib: A 2D graphics environment. *Computing in Science & Engineering*,  
1072 **9** (3), 90–95, <https://doi.org/10.1109/MCSE.2007.55>.
- 1073 Illingworth, A. J., J. W. F. Goddard, and S. M. Cherry, 1987: Polarization radar studies of  
1074 precipitation development in convective storms. *Q. J. R. Meteorolog. Soc.*, **113** (476), 469–489,  
1075 <https://doi.org/10.1002/qj.49711347604>.
- 1076 Johnson, D. B., 1987: On the relative efficiency of coalescence and riming. *Journal of Atmo-*  
1077 *spheric Sciences*, **44** (13), 1671 – 1680, [https://doi.org/10.1175/1520-0469\(1987\)044<1671:OTREOC>2.0.CO;2](https://doi.org/10.1175/1520-0469(1987)044<1671:OTREOC>2.0.CO;2), URL [https://journals.ametsoc.org/view/journals/atsc/44/13/1520-0469-1987\\_044\\_1671\\_otreoc\\_2\\_0\\_co\\_2.xml](https://journals.ametsoc.org/view/journals/atsc/44/13/1520-0469-1987_044_1671_otreoc_2_0_co_2.xml).
- 1080 King, J. R., M. D. Parker, K. D. Sherburn, and G. M. Lackmann, 2017: Rapid Evolution of Cool  
1081 Season, Low-CAPE Severe Thunderstorm Environments. *Wea. Forecasting*, **32** (2), 763–779,  
1082 <https://doi.org/10.1175/WAF-D-16-0141.1>.

- 1083 Knight, C. A., 2006: Very Early Formation of Big, Liquid Drops Revealed by ZDR in Continental  
1084 Cumulus. *J. Atmos. Sci.*, **63** (7), 1939–1953, <https://doi.org/10.1175/JAS3721.1>.
- 1085 Koch, S. E., M. desJardins, and P. J. Kocin, 1983: An interactive barnes objective map anal-  
1086 ysis scheme for use with satellite and conventional data. *J. Appl. Meteor. Climatol.*, **22** (9),  
1087 1487 – 1503, [https://doi.org/10.1175/1520-0450\(1983\)022<1487:AIBOMA>2.0.CO;2](https://doi.org/10.1175/1520-0450(1983)022<1487:AIBOMA>2.0.CO;2), URL [https://journals.ametsoc.org/view/journals/apme/22/9/1520-0450\\_1983\\_022\\_1487\\_aiboma\\_2\\_0\\_co\\_2.xml](https://journals.ametsoc.org/view/journals/apme/22/9/1520-0450_1983_022_1487_aiboma_2_0_co_2.xml).
- 1090 Koshak, W. J., and Coauthors, 2004: North Alabama Lightning Mapping Array (LMA): VHF  
1091 Source Retrieval Algorithm and Error Analyses. *J. Atmos. Oceanic Technol.*, **21** (4), 543–558,  
1092 [https://doi.org/10.1175/1520-0426\(2004\)021<0543:NALMAL>2.0.CO;2](https://doi.org/10.1175/1520-0426(2004)021<0543:NALMAL>2.0.CO;2).
- 1093 Krause, J., and V. Klaus, 2024: Identifying zdr columns in radar data with the hotspot  
1094 technique. *Weather and Forecasting*, <https://doi.org/10.1175/WAF-D-23-0146.1>, URL <https://journals.ametsoc.org/view/journals/wefo/aop/WAF-D-23-0146.1/WAF-D-23-0146.1.xml>.
- 1096 Kuettner, J. P., J. D. Sartor, and Z. Levin, 1981: Thunderstorm electrification—inductive or  
1097 non-inductive? *Journal of the Atmospheric Sciences*, **38** (11), 2470–2484.
- 1098 Kumjian, M. R., S. M. Ganson, and A. V. Ryzhkov, 2012: Freezing of raindrops in deep  
1099 convective updrafts: A microphysical and polarimetric model. *J. Atmos. Sci.*, **69** (12), 3471  
1100 – 3490, [https://doi.org/https://doi.org/10.1175/JAS-D-12-067.1](https://doi.org/10.1175/JAS-D-12-067.1), URL <https://journals.ametsoc.org/view/journals/atsc/69/12/jas-d-12-067.1.xml>.
- 1102 Kumjian, M. R., A. P. Khain, N. Benmoshe, E. Ilotoviz, A. V. Ryzhkov, and V. T. J. Phillips, 2014:  
1103 The Anatomy and Physics of ZDR Columns: Investigating a Polarimetric Radar Signature  
1104 with a Spectral Bin Microphysical Model. *J. Appl. Meteor. Climatol.*, **53** (7), 1820–1843,  
1105 <https://doi.org/10.1175/JAMC-D-13-0354.1>.
- 1106 Kumjian, M. R., S. Mishra, S. E. Giangrande, T. Toto, A. V. Ryzhkov, and A. Bansemer, 2016:  
1107 Polarimetric radar and aircraft observations of saggy bright bands during MC3E. *J. Geophys. Res.*  
1108 *Atmos.*, **121** (7), 3584–3607, <https://doi.org/10.1002/2015JD024446>, URL <https://onlinelibrary.wiley.com/doi/abs/10.1002/2015JD024446>.

- 1110 Kumjian, M. R., and A. V. Ryzhkov, 2008: Polarimetric Signatures in Supercell Thunderstorms.  
1111 *J. Appl. Meteor. Climatol.*, **47** (7), 1940–1961, <https://doi.org/10.1175/2007JAMC1874.1>.
- 1112 Kumjian, M. R., A. V. Ryzhkov, V. M. Melnikov, and T. J. Schuur, 2010: Rapid-scan super-  
1113 resolution observations of a cyclic supercell with a dual-polarization wsr-88d. *Mon. Wea. Rev.*,  
1114 **138** (10), 3762 – 3786, [https://doi.org/https://doi.org/10.1175/2010MWR3322.1](https://doi.org/10.1175/2010MWR3322.1), URL <https://journals.ametsoc.org/view/journals/mwre/138/10/2010mwr3322.1.xml>.
- 1115  
1116 Kuster, C. M., B. R. Bowers, J. T. Carlin, T. J. Schuur, J. W. Brogden, R. Toomey, and A. Dean,  
1117 2021: Using kdp cores as a downburst precursor signature. *Weather and Forecasting*, **36** (4),  
1118 1183 – 1198, <https://doi.org/10.1175/WAF-D-21-0005.1>, URL <https://journals.ametsoc.org/>  
1119 view/journals/wefo/36/4/WAF-D-21-0005.1.xml.
- 1120 Kuster, C. M., T. J. Schuur, T. T. Lindley, and J. C. Snyder, 2020: Using ZDR Columns in  
1121 Forecaster Conceptual Models and Warning Decision-Making. *Wea. Forecasting*, **35** (6), 2507–  
1122 2522, <https://doi.org/10.1175/WAF-D-20-0083.1>.
- 1123 Kuster, C. M., J. C. Snyder, T. J. Schuur, T. T. Lindley, P. L. Heinzelman, J. C. Furtado, J. W.  
1124 Brogden, and R. Toomey, 2019: Rapid-Update Radar Observations of ZDR Column Depth and  
1125 Its Use in the Warning Decision Process. *Wea. Forecasting*, **34** (4), 1173–1188, <https://doi.org/10.1175/WAF-D-19-0024.1>.
- 1126  
1127 Latham, J., and J. E. Dye, 1989: Calculations on the electrical development of a small thunderstorm.  
1128 *J. Geophys. Res.: Atmos.*, **94** (D11), 13 141–13 144, <https://doi.org/10.1029/JD094iD11p13141>.
- 1129 Lewiner, T., H. Lopes, A. W. Vieira, and G. Tavares, 2003: Efficient Implementation of Marching  
1130 Cubes' Cases with Topological Guarantees. *J. Graphics Tools*, **8** (2), 1–15, <https://doi.org/10.1080/10867651.2003.10487582>.
- 1131  
1132 Loeffler, S. D., and M. R. Kumjian, 2020: Idealized Model Simulations to Determine Impacts  
1133 of Storm-Relative Winds on Differential Reflectivity and Specific Differential Phase Fields. *J.*  
1134 *Geophys. Res. Atmos.*, **125** (24), e2020JD033 870, <https://doi.org/10.1029/2020JD033870>.
- 1135  
1136 Loney, M. L., D. S. Zrnić, J. M. Straka, and A. V. Ryzhkov, 2002: Enhanced Polarimetric Radar  
1137 Signatures above the Melting Level in a Supercell Storm. *J. Appl. Meteor. Climatol.*, **41** (12),  
1179–1194, [https://doi.org/10.1175/1520-0450\(2002\)041<1179:EPRSAT>2.0.CO;2](https://doi.org/10.1175/1520-0450(2002)041<1179:EPRSAT>2.0.CO;2).

- 1138 MacGorman, D. R., I. R. Apostolakopoulos, N. R. Lund, N. W. S. Demetriades, M. J. Mur-  
1139 phy, and P. R. Krehbiel, 2011: The timing of cloud-to-ground lightning relative to total  
1140 lightning activity. *Mon. Wea. Rev.*, **139** (12), 3871 – 3886, <https://doi.org/https://doi.org/10.1175/MWR-D-11-00047.1>, URL <https://journals.ametsoc.org/view/journals/mwre/139/12/mwr-d-11-00047.1.xml>.  
1141  
1142
- 1143 MacGorman, D. R., and D. W. Burgess, 1994: Positive Cloud-to-Ground Lightning in Tor-  
1144 nadic Storms and Hailstorms. *Mon. Wea. Rev.*, **122** (8), 1671–1697, [https://doi.org/10.1175/1520-0493\(1994\)122<1671:PCTGLI>2.0.CO;2](https://doi.org/10.1175/1520-0493(1994)122<1671:PCTGLI>2.0.CO;2).  
1145  
1146 MacGorman, D. R., and Coauthors, 2008: TELEX The Thunderstorm Electrification and  
1147 Lightning Experiment. *Bull. Amer. Meteor. Soc.*, **89** (7), 997–1014, <https://doi.org/10.1175/2007BAMS2352.1>.  
1148  
1149 Majcen, M., P. Markowski, Y. Richardson, D. Dowell, and J. Wurman, 2008: Multipass Ob-  
1150 jective Analyses of Doppler Radar Data. *J. Atmos. Oceanic Technol.*, **25** (10), 1845–1858,  
1151 <https://doi.org/10.1175/2008JTECHA1089.1>.  
1152  
1153 Mallick, S., and Coauthors, 2014: Performance characteristics of the NLDN for return strokes  
1154 and pulses superimposed on steady currents, based on rocket-triggered lightning data acquired  
1155 in Florida in 2004–2012: Evaluation of NLDN Performance. *J. Geophys. Res. Atmos.*, **119** (7),  
1156 3825–3856, <https://doi.org/10.1002/2013JD021401>.  
1157  
1158 Marshall, T. C., W. D. Rust, and M. Stolzenburg, 1995: Electrical structure and updraft speeds  
1159 in thunderstorms over the southern Great Plains. *J. Geophys. Res. Atmospheres*, **100** (D1),  
1160 1001–1015, <https://doi.org/10.1029/94JD02607>.  
1161  
1162 May, R. M., S. C. Arms, P. Marsh, E. Bruning, J. R. Leeman, K. Goebbert, J. E. Thielen, and Z. S.  
1163 Bruick, 2008: MetPy: A Python Package for Meteorological Data. Boulder, Colorado, Unidata,  
1164 <https://doi.org/10.5065/D6WW7G29>.  
1165  
1166 McDonald, J. R., and K. C. Mehta, 2004: A Recommendation for an Enhanced Fujita Scale (EF-  
1167 Scale). Tech. Rep. 602, Wind Science and Engineering Center, Texas Tech University, Lubbock,  
1168 Texas, 95 pp.  
1169

- 1165 Mecikalski, J. R., T. N. Sandmæl, E. M. Murillo, C. R. Homeyer, K. M. Bedka, J. M. Apke,  
1166 and C. P. Jewett, 2021: A random-forest model to assess predictor importance and nowcast  
1167 severe storms using high-resolution radar–goes satellite–lightning observations. *Mon. Wea. Rev.*,  
1168 **149** (6), 1725 – 1746, <https://doi.org/10.1175/MWR-D-19-0274.1>, URL <https://journals.ametsoc.org/view/journals/mwre/149/6/MWR-D-19-0274.1.xml>.
- 1170 Montopoli, M., E. Picciotti, L. Baldini, S. Di Fabio, F. Marzano, and G. Vulpiani, 2021: Gazing  
1171 inside a giant-hail-bearing mediterranean supercell by dual-polarization doppler weather radar.  
1172 *Atmos. Res.*, **264**, 105 852, <https://doi.org/10.1016/j.atmosres.2021.105852>, URL  
1173 <https://www.sciencedirect.com/science/article/pii/S0169809521004087>.
- 1174 Morrison, H., and Coauthors, 2020: Confronting the Challenge of Modeling Cloud and Pre-  
1175 cipitation Microphysics. *J. Adv. Model. Earth Syst.*, **12** (8), e2019MS001 689, <https://doi.org/10.1029/2019MS001689>.
- 1177 Murphy, M. J., J. A. Cramer, and R. K. Said, 2021: Recent History of Upgrades to the U.S. National  
1178 Lightning Detection Network. *J. Atmos. Oceanic Technol.*, **38** (3), 573–585, <https://doi.org/10.1175/JTECH-D-19-0215.1>.
- 1180 NCEI report, 2016: NCEI Storm Events Database. National Centers for Environmental Information,  
1181 <https://www.ncdc.noaa.gov/stormevents/eventdetails.jsp?id=623795>.
- 1182 Nixon, C. J., and J. T. Allen, 2022: Distinguishing between Hodographs of Severe Hail and  
1183 Tornadoes. *Wea. Forecasting*, **37** (10), 1761–1782, <https://doi.org/10.1175/WAF-D-21-0136.1>.
- 1184 NOAA, National Centers for Environmental Information, 2022: NOAA National Weather Service  
1185 (NWS) Radar Operations Center (1991): NOAA Next Generation Radar (NEXRAD) Level 2  
1186 Base Data.
- 1187 NOAA National Weather Service (NWS) Radar Operations Center, 1991: NOAA Next Generation  
1188 Radar (NEXRAD) Level 2 Base Data. [KHTX]. NOAA National Centers for Environmental  
1189 Information, <https://doi.org/10.7289/V5W9574V>.
- 1190 Orville, R. E., 2008: Development of the National Lightning Detection Network. *Bull. Amer.*  
1191 *Meteor. Soc.*, **89** (2), 180–190, <https://doi.org/10.1175/BAMS-89-2-180>.

- 1192 Petersen, W. A., H. J. Christian, and S. A. Rutledge, 2005a: TRMM observations of the global  
1193 relationship between ice water content and lightning. *Geophys. Res. Lett.*, **32** (14), <https://doi.org/10.1029/2005GL023236>.
- 1195 Petersen, W. A., K. Knupp, J. Walters, R. Blakeslee, W. Deierling, M. Newchurch, and R. McNider,  
1196 2005b: THE NSSTC ARMOR C-BAND DUAL-POLARIMETRIC DOPPLER RADAR: A  
1197 TOOL FOR INTEGRATED REMOTE SENSING. *Huntsville Simulation Conference*, Society  
1198 for Modeling and Simulation International, Huntsville, Alabama, 5.
- 1199 Phillips, V. T., 2024: A theory for the balance between warm rain and ice crystal processes of  
1200 precipitation in mixed-phase clouds. *Journal of the Atmospheric Sciences*, **81** (2), 317–339.
- 1201 Picca, J. C., 2010: Z<sub>DR</sub> columns as a predictive tool for hail growth and storm evolution. *25th*  
1202 *Conference on Severe Local Storms (11 - 14 October 2010)*, AMS.
- 1203 Plummer, D. M., and Coauthors, 2018: Radar-Derived Structural and Precipitation Characteristics  
1204 of ZDR Columns within Warm-Season Convection over the United Kingdom. *J. Appl. Meteor.*  
1205 *Climatol.*, **57** (11), 2485–2505, <https://doi.org/10.1175/JAMC-D-17-0134.1>.
- 1206 Proctor, D. E., 1971: A hyperbolic system for obtaining VHF radio pictures of lightning. *J.*  
1207 *Geophys. Res.*, **76** (6), 1478–1489, <https://doi.org/10.1029/JC076i006p01478>.
- 1208 Proctor, D. E., R. Uytenbogaardt, and B. M. Meredith, 1988: VHF radio pictures of lightning  
1209 flashes to ground. *J. Geophys. Res. Atmos.*, **93** (D10), 12 683–12 727, <https://doi.org/10.1029/JD093iD10p12683>.
- 1211 Reimel, K. J., and M. Kumjian, 2021: Evaluation of KDP Estimation Algorithm Performance  
1212 in Rain Using a Known-Truth Framework. *J. Atmos. Oceanic Technol.*, **38** (3), 587–605,  
1213 <https://doi.org/10.1175/JTECH-D-20-0060.1>.
- 1214 Reynolds, S., M. Brook, and M. F. Gourley, 1957: Thunderstorm charge separation. *Journal of*  
1215 *Atmospheric Sciences*, **14** (5), 426–436.
- 1216 Rison, W., R. J. Thomas, P. R. Krehbiel, T. Hamlin, and J. Harlin, 1999: A GPS-based three-  
1217 dimensional lightning mapping system: Initial observations in central New Mexico. *Geophys.*  
1218 *Res. Lett.*, **26** (23), 3573–3576, <https://doi.org/10.1029/1999GL010856>.

- <sub>1219</sub> Ryzhkov, A. V., V. B. Zhuravlyov, and N. A. Rybakova, 1994: Preliminary Results of X-Band  
<sub>1220</sub> Polarization Radar Studies of Clouds and Precipitation. *J. Atmos. Oceanic Technol.*, **11** (1),  
<sub>1221</sub> 132–139, [https://doi.org/10.1175/1520-0426\(1994\)011<0132:PROXBP>2.0.CO;2](https://doi.org/10.1175/1520-0426(1994)011<0132:PROXBP>2.0.CO;2).
- <sub>1222</sub> Ryzhkov, A. V., and D. S. Zrnic, 1998: Polarimetric Rainfall Estimation in the Presence of  
<sub>1223</sub> Anomalous Propagation. *J. Atmos. Oceanic Technol.*, **15** (6), 1320–1330, [https://doi.org/10.1175/1520-0426\(1998\)015<1320:PREITP>2.0.CO;2](https://doi.org/10.1175/1520-0426(1998)015<1320:PREITP>2.0.CO;2).
- <sub>1225</sub> Salinas, V., E. C. Bruning, and E. R. Mansell, 2022: Examining the Kinematic Structures within  
<sub>1226</sub> which Lightning Flashes Are Initiated Using a Cloud-Resolving Model. *J. Atmos. Sci.*, **79** (2),  
<sub>1227</sub> 513–530, <https://doi.org/10.1175/JAS-D-21-0132.1>.
- <sub>1228</sub> Sandmæl, T. N., C. R. Homeyer, K. M. Bedka, J. M. Apke, J. R. Mecikalski, and K. Khlopenkov,  
<sub>1229</sub> 2019: Evaluating the ability of remote sensing observations to identify significantly severe and  
<sub>1230</sub> potentially tornadic storms. *J. Appl. Meteor. Climatol.*, **58** (12), 2569 – 2590, <https://doi.org/https://doi.org/10.1175/JAMC-D-18-0241.1>, URL <https://journals.ametsoc.org/view/journals/apme/58/12/jamc-d-18-0241.1.xml>.
- <sub>1233</sub> Scharfenberg, K. A., and Coauthors, 2005: The Joint Polarization Experiment: Polarimetric Radar  
<sub>1234</sub> in Forecasting and Warning Decision Making. *Wea. Forecasting*, **20** (5), 775–788, <https://doi.org/10.1175/WAF881.1>.
- <sub>1236</sub> Schlatter, P., 2003: Polarimetric radar and in-situ measurements of a nontornadic supercell. M.S.  
<sub>1237</sub> thesis, School of Meteorology, University of Oklahoma, Norman, OK.
- <sub>1238</sub> Schneider, R. S., and A. R. Dean, 2008: A Comprehensive 5-Year Severe Storm Environment  
<sub>1239</sub> Climatology for the Continental United States. *Session 16A, Severe Weather Climatology I*,  
<sub>1240</sub> American Meteorological Society, Savannah, GA, Vol. 16A.4, 9, URL [https://ams.confex.com/ams/24SLS/techprogram/paper\\_141748.htm](https://ams.confex.com/ams/24SLS/techprogram/paper_141748.htm).
- <sub>1242</sub> Schultz, C. J., L. D. Carey, E. V. Schultz, and R. J. Blakeslee, 2015: Insight into the Kinematic and  
<sub>1243</sub> Microphysical Processes that Control Lightning Jumps. *Wea. Forecasting*, **30** (6), 1591–1621,  
<sub>1244</sub> <https://doi.org/10.1175/WAF-D-14-00147.1>.

- 1245 Segall, J. H., M. M. French, D. M. Kingfield, S. D. Loeffler, and M. R. Kumjian, 2022: Storm-  
1246 Scale Polarimetric Radar Signatures Associated with Tornado Dissipation in Supercells. *Wea.*  
1247 *Forecasting*, **37** (1), 3–21, <https://doi.org/10.1175/WAF-D-21-0067.1>.
- 1248 Sharma, M., R. L. Tanamachi, E. C. Bruning, and K. M. Calhoun, 2021: Polarimetric and Electrical  
1249 Structure of the 19 May 2013 Edmond–Carney, Oklahoma, Tornadic Supercell. *Mon. Wea. Rev.*,  
1250 **149** (7), 2049–2078, <https://doi.org/10.1175/MWR-D-20-0280.1>.
- 1251 Sherburn, K. D., and M. D. Parker, 2014: Climatology and Ingredients of Significant Severe  
1252 Convection in High-Shear, Low-CAPE Environments. *Wea. Forecasting*, **29** (4), 854–877,  
1253 <https://doi.org/10.1175/WAF-D-13-00041.1>.
- 1254 Sherburn, K. D., M. D. Parker, J. R. King, and G. M. Lackmann, 2016: Composite Environments  
1255 of Severe and Nonsevere High-Shear, Low-CAPE Convective Events. *Wea. Forecasting*, **31** (6),  
1256 1899–1927, <https://doi.org/10.1175/WAF-D-16-0086.1>.
- 1257 Sinclair, V. A., D. Moisseev, and A. von Lerber, 2016: How dual-polarization radar observations  
1258 can be used to verify model representation of secondary ice. *Journal of Geophysical Research:*  
1259 *Atmospheres*, **121** (18), 10,954–10,970, <https://doi.org/10.1002/2016JD025381>, URL <https://onlinelibrary.wiley.com/doi/abs/10.1002/2016JD025381>.
- 1261 Smith, P. L., D. J. Musil, A. G. Detwiler, and R. Ramachandran, 1999: Observations of Mixed-  
1262 Phase Precipitation within a CaPE Thunderstorm. *J. Appl. Meteor. Climatol.*, **38** (2), 145–155,  
1263 [https://doi.org/10.1175/1520-0450\(1999\)038<0145:OOMPPW>2.0.CO;2](https://doi.org/10.1175/1520-0450(1999)038<0145:OOMPPW>2.0.CO;2).
- 1264 Snyder, J. C., H. B. Bluestein, D. T. D. Ii, and Y. Jung, 2017: Simulations of Polarimetric, X-Band  
1265 Radar Signatures in Supercells. Part II: ZDR Columns and Rings and KDP Columns. *J. Appl.*  
1266 *Meteor. Climatol.*, **56** (7), 2001–2026, <https://doi.org/10.1175/JAMC-D-16-0139.1>.
- 1267 Snyder, J. C., H. B. Bluestein, V. Venkatesh, and S. J. Frasier, 2013: Observations of Polarimetric  
1268 Signatures in Supercells by an X-Band Mobile Doppler Radar. *Mon. Wea. Rev.*, **141** (1), 3–29,  
1269 <https://doi.org/10.1175/MWR-D-12-00068.1>.
- 1270 Snyder, J. C., A. V. Ryzhkov, M. R. Kumjian, A. P. Khain, and J. Picca, 2015: A ZDR Column  
1271 Detection Algorithm to Examine Convective Storm Updrafts. *Wea. Forecasting*, **30** (6), 1819–  
1272 1844, <https://doi.org/10.1175/WAF-D-15-0068.1>.

- 1273 Souza, J. C. S., and E. C. Bruning, 2021: Assessment of Turbulence Intensity in Different Spots  
1274 of Lightning Flash Propagation. *Geophys. Res. Lett.*, **48** (21), e2021GL095 923, <https://doi.org/10.1029/2021GL095923>.
- 1275
- 1276 Stough, S. M., L. D. Carey, C. J. Schultz, and D. J. Cecil, 2021: Examining Conditions Sup-  
1277 porting the Development of Anomalous Charge Structures in Supercell Thunderstorms in the  
1278 Southeastern United States. *J. Geophys. Res. Atmos.*, **126** (16), e2021JD034 582, <https://doi.org/10.1029/2021JD034582>.
- 1279
- 1280 Stough, S. M., L. D. Carey, C. J. Schultz, and D. J. Cecil, 2022: Supercell Thunderstorm Charge  
1281 Structure Variability and Influences on Spatial Lightning Flash Relationships with the Updraft.  
1282 *Mon. Wea. Rev.*, **150** (4), 843–861, <https://doi.org/10.1175/MWR-D-21-0071.1>.
- 1283
- 1284 Strapp, J., and Coauthors, 2016: The high ice water content study of deep convective clouds:  
Report on science and technical plan. *Tech. Rep. DOT/FAA/TC-14/31*.
- 1285
- 1286 Takahashi, T., 1978: Riming electrification as a charge generation mechanism in thunderstorms.  
*Journal of Atmospheric Sciences*, **35** (8), 1536–1548.
- 1287
- 1288 Thomas, R. J., P. R. Krehbiel, W. Rison, S. J. Hunyady, W. P. Winn, T. Hamlin, and J. Harlin, 2004:  
Accuracy of the Lightning Mapping Array. *J. Geophys. Res. Atmos.*, **109** (D14), <https://doi.org/10.1029/2004JD004549>.
- 1289
- 1290 Van Den Broeke, M. S., 2016: Polarimetric Variability of Classic Supercell Storms as a  
1291 Function of Environment. *J. Appl. Meteor. Climatol.*, **55** (9), 1907–1925, <https://doi.org/10.1175/JAMC-D-15-0346.1>.
- 1292
- 1293 Van Den Broeke, M. S., 2017: Polarimetric Radar Metrics Related to Tornado Life Cycles and  
1294 Intensity in Supercell Storms. *Mon. Wea. Rev.*, **145** (9), 3671–3686, <https://doi.org/10.1175/MWR-D-16-0453.1>.
- 1295
- 1296 Van Den Broeke, M. S., 2020: A Preliminary Polarimetric Radar Comparison of Pretornadic and  
1297 Nontornadic Supercell Storms. *Mon. Wea. Rev.*, **148** (4), 1567–1584, <https://doi.org/10.1175/MWR-D-19-0296.1>.
- 1298
- 1299 van der Walt, S., and Coauthors, 2014: Scikit-image: Image processing in Python. *PeerJ*, **2**, e453,  
1300 <https://doi.org/10.7717/peerj.453>.

- 1301 van Lier-Walqui, M., and Coauthors, 2016: On Polarimetric Radar Signatures of Deep Convection  
1302 for Model Evaluation: Columns of Specific Differential Phase Observed during MC3E. *Mon.*  
1303 *Wea. Rev.*, **144** (2), 737–758, <https://doi.org/10.1175/MWR-D-15-0100.1>.
- 1304 Virtanen, P., and Coauthors, 2020: SciPy 1.0: Fundamental algorithms for scientific computing in  
1305 python. *Nat. Methods*, **17**, 261–272, <https://doi.org/10.1038/s41592-019-0686-2>.
- 1306 VSE report, 2017: VORTEX-SE 2017 Damage Survey Report. Available at  
1307 [http://catalog.eol.ucar.edu/vortex-se\\_2017/report/67/1333/200005/54412852](http://catalog.eol.ucar.edu/vortex-se_2017/report/67/1333/200005/54412852).
- 1308 Waitz, F., M. Schnaiter, T. Leisner, and E. Järvinen, 2022: In situ observation of riming in mixed-  
1309 phase clouds using the PHIPS probe. *Atmospheric Chemistry and Physics*, **22** (11), 7087–  
1310 7103, <https://doi.org/10.5194/acp-22-7087-2022>, URL <https://acp.copernicus.org/articles/22/7087/2022/>.
- 1312 Weiss, S. A., D. R. MacGorman, E. C. Bruning, and V. C. Chmielewski, 2018: Two Methods  
1313 for Correcting Range-Dependent Limitations of Lightning Mapping Arrays. *J. Atmos. Oceanic  
1314 Technol.*, **35** (6), 1273–1282, <https://doi.org/10.1175/JTECH-D-17-0213.1>.
- 1315 Wienhoff, Z. B., H. B. Bluestein, L. J. Wicker, J. C. Snyder, A. Shapiro, C. K. Potvin, J. B. Houser,  
1316 and D. W. Reif, 2018: Applications of a Spatially Variable Advection Correction Technique  
1317 for Temporal Correction of Dual-Doppler Analyses of Tornadic Supercells. *Mon. Wea. Rev.*,  
1318 **146** (9), 2949–2971, <https://doi.org/10.1175/MWR-D-17-0360.1>.
- 1319 Wiens, K. C., S. A. Rutledge, and S. A. Tessendorf, 2005: The 29 June 2000 Supercell Observed  
1320 during STEPS. Part II: Lightning and Charge Structure. *J. Atmos. Sci.*, **62** (12), 4151–4177,  
1321 <https://doi.org/10.1175/JAS3615.1>.
- 1322 Williams, E. R., 1985: Large-scale charge separation in thunderclouds. *J. Geophys. Res. Atmos.*,  
1323 **90** (D4), 6013–6025, <https://doi.org/10.1029/JD090iD04p06013>.
- 1324 Wilson, M. B., and M. S. Van Den Broeke, 2022: Using the Supercell Polarimetric Observation  
1325 Research Kit (SPORK) to Examine a Large Sample of Pretornadic and Nontornadic Supercells.  
1326 *Electron. J. Severe Storms Metereol.*, **17** (2), 1–38, <https://doi.org/10.55599/ejssm.v17i2.85>.
- 1327 Zrnić, D. S., 1987: Three-body scattering produces precipitation signature of special diagnostic  
1328 value. *Radio Sci.*, **22** (1), 76–86, <https://doi.org/10.1029/RS022i001p00076>.